

Published in final edited form as:

Nature. 2019 September 01; 573(7773): 287–290. doi:10.1038/s41586-019-1530-7.

Influenza A virus RNA polymerase structures provide insights into viral genome replication

Haitian Fan^{#1}, Alexander P Walker^{#1}, Loïc Carrique^{#2}, Jeremy R Keown^{#2}, Itziar Serna Martin^{1,2,6}, Dimple Karia², Jane Sharps¹, Narin Hengrung^{1,2,7}, Els Pardon³, Jan Steyaert⁴, Jonathan M Grimes^{2,5,9,*}, Ervin Fodor^{1,9,*}

¹Sir William Dunn School of Pathology, University of Oxford, South Parks Road, Oxford OX1 3RE, United Kingdom

²Division of Structural Biology, Henry Wellcome Building for Genomic Medicine, University of Oxford, Oxford OX3 7BN, United Kingdom

³VIB-VUB Center for Structural Biology, VIB, 1050 Brussels, Belgium

⁴Structural Biology Brussels, Vrije Universiteit Brussel, 1050 Brussels, Belgium

⁵Diamond Light Source Ltd, Harwell Science & Innovation Campus, Didcot OX11 0DE, United Kingdom

These authors contributed equally to this work.

Abstract

Influenza A viruses (IAV) are responsible for seasonal epidemics, and pandemics can arise from novel zoonotic influenza A viruses transmitting to humans^{1,2}. IAV contain a segmented negative sense RNA genome that is transcribed and replicated by the viral RNA-dependent RNA polymerase, composed of the PB1, PB2, and PA subunits^{3–5}. Although the high-resolution crystal structure of bat IAV polymerase (FluPol_A) has been reported⁶, there are no complete structures available for human and avian FluPol_A. Furthermore, the molecular mechanisms of viral RNA (vRNA) replication, which proceeds through a complementary RNA (cRNA) replicative intermediate and requires polymerase oligomerisation^{7–10}, remain largely unknown. Here we

Users may view, print, copy, and download text and data-mine the content in such documents, for the purposes of academic research, subject always to the full Conditions of use:http://www.nature.com/authors/editorial_policies/license.html#terms

* **Correspondence and requests for materials** should be addressed to J.M.G. or E.F. jonathan@strubi.ox.ac.uk, ervin.fodor@path.ox.ac.uk.

⁶Present address: Crystal and Structural Chemistry, Bijvoet Center for Biomolecular Research, Department of Chemistry, Faculty of Science, Utrecht University, Padualaan 8, 3584 CH, Utrecht, The Netherlands

⁷Present address: Francis Crick Institute, 1 Midland Road, Kings Cross, London NW1 1AT, United Kingdom

⁹These authors jointly supervised this work: Jonathan M Grimes, Ervin Fodor

Author contributions

H.F., A.P.W., L.C., J.R.K., J.M.G. and E.F. conceived and designed the study. H.F., L.C., J.R.K., and N.H. carried out cloning of recombinant baculoviruses and protein purification. H.F. J.R.K. performed crystallisations, data collection and analysis, model building and refinement. L.C. and J.R.K. collected and processed electron microscopy data and built and refined models with assistance from D.K. and I.S.M. A.P.W. performed functional assays and analysed data. J.S. performed dimerisation assays in mammalian cells and E.F. analysed the data. E.P. and J.S. designed and generated Nb8205 and Nb8210 and N.H. performed nanobody expression and purification. J.M.G. and E.F. supervised the structural and functional studies, respectively. H.F., A.P.W., L.C., J.R.K., J.M.G. and E.F. wrote the manuscript, with input from all co-authors.

Competing interests The authors declare no competing interests.

report 3.0 – 4.3 Å resolution structures of polymerases from human A/NT/60/1968 (H3N2) and avian A/duck/Fujian/01/2002 (H5N1) IAVs, obtained by crystallography and cryo-electron microscopy (cryo-EM), in the presence or absence of cRNA or vRNA template. In solution, FluPol_A forms dimers of heterotrimers through the PA C-terminal domain and the PB1 thumb and PB2 N1 subdomains. A cryo-EM structure of a monomeric FluPol_A, bound to cRNA template, reveals a binding site for the 3' cRNA at the dimer interface. Using a combination of cell-based and *in vitro* assays we show that the FluPol_A dimer interface is required for initiation of vRNA synthesis during viral genome replication. Furthermore, we show that a nanobody, a single-domain antibody, which interferes with FluPol_A dimerisation, inhibits vRNA synthesis and consequently virus replication in infected cells. Our study provides the first high-resolution structures of medically relevant FluPol_A and offers novel insights into the replication mechanisms of the viral RNA genome. Furthermore, it identifies novel sites of FluPol_A that could be targeted for antiviral drug development.

We used x-ray crystallography to solve the complete apo structures of human and avian FluPol_A at 3.32 Å and 3.63 Å resolution, respectively (Extended Data Fig. 1a-f, Extended Data Table 1, Supplementary Fig. 1). Human and avian FluPol_A are essentially identical structures forming dimers of heterotrimers with dimerisation mediated by the PA C-terminal domain, the PB1 thumb and PB2 N1 subdomains (Fig. 1a, b, Extended Data Fig. 1g-i). A key feature of this dimer interface is loop 352-356 in the PA C-terminal domain that interacts with the same loop of the second polymerase (Fig. 1c, Extended Data Fig. 1g). The dimer interface also involves hydrogen bonds between the PA C-terminal domain and PB2 N1 (Fig. 1d, Extended Data Fig. 1h). Mutation of PA residues 352-356 to alanines (PA_{352-356A}) resulted in a shift towards a monomeric FluPol_A heterotrimer (Extended Data Fig. 2a). FluPol_A dimerisation through the same interface was also observed in mammalian cells (Extended Data Fig. 2b) and in previous studies of a truncated avian FluPol_A¹¹.

To assess the importance of dimerisation for FluPol_A function we used a minireplicon assay measuring viral transcription and replication in the context of viral ribonucleoprotein complexes (vRNPs) (Fig. 2a). The PA_{352-356A} dimer interface mutation and mutations designed to destabilise PB2 loop 71-76 and PA loop 352-356 at the dimer interface significantly decreased the synthesis of all viral RNAs (Fig. 2b, Extended Data Fig. 2c). Co-expression of PA_{352-356A} with PA_{D108A}, a transcription-deficient but replication-competent polymerase^{12,13}, lead to a significant increase in mRNA signal, indicating that the PA_{352-356A} mutant is specifically deficient in viral genome replication (Fig. 2b). In agreement, the PA_{352-356A} mutation did not inhibit transcription *in vitro* using a vRNA template and capped RNA primer (Fig. 2c). It did not affect primer-independent cRNA synthesis on a vRNA template either but was deficient in vRNA synthesis on a cRNA template (Fig. 2d, e) that involves pppApG synthesis at positions 4 and 5 and subsequent realignment of the template¹⁴. In ApG dinucleotide-primed assays, the PA_{352-356A} mutant showed activity on both vRNA and cRNA templates but on the cRNA template promoted the formation of a short 12 nucleotide and other incorrectly initiated products (Extended Fig. 2d, e). The ratio of full-length 15 to the short 12 nucleotide product was dependent on FluPol_A concentration, and could be increased by adding a polymerase active site mutant (PB1a), suggesting the involvement of an intermolecular interaction between polymerases (Extended

Data Fig. 2f, g). These data show that the FluPol_A dimer interface is important for initiation of vRNA synthesis on the cRNA template and suggest that dimerisation promotes stabilisation of the replication complex and the correct positioning of the cRNA template to allow terminal pppApG-primed initiation during vRNA synthesis.

To investigate the binding of FluPol_A to the cRNA template we determined the structure of dimeric FluPol_A in the presence of cRNA promoter (comprised of 5' and 3' cRNA termini)^{3,4} at 4.07 Å resolution using cryo-EM (Fig. 3a, Extended Data Fig. 3a-f, Extended Data Table 2). Although the PA endonuclease and PB2 C-terminal domains could not be resolved, in agreement with previous observations that these domains are flexible¹⁵⁻¹⁷, unambiguous density was observed for the dimer interface, revealing a dimer interface essentially identical to that in the FluPol_A crystal structures (Fig. 1a). Only the 5' cRNA was clearly resolved in the density maps, showing a hook structure bound in a pocket formed by PA and PB1, as observed in previous FluPol structures with 5' vRNA and cRNA^{6,16,18}. Unresolved density around the template entry channel was observed suggesting that the 3' cRNA has entered the active site but is highly dynamic (Extended Data Fig. 3g, h). These results confirm that cRNA-bound FluPol_A can form dimers in solution.

To gain further insight into FluPol_A dimerisation and cRNA binding we used a nanobody (Nb8205) raised against FluPol_A that reduces FluPol_A dimerisation (Extended Data Fig. 4a-c). A crystal structure of the apo FluPol_A-Nb8205 complex solved at 3.34 Å resolution revealed that the complementarity determining regions (CDRs) of Nb8205 interact with FluPol_A at the PA C-terminal domain and PB1 thumb, a site close to the dimer interface (Extended Data Fig. 4d, e, Extended Data Table 1). We also solved the structures of monomeric and dimeric FluPol_A bound to Nb8205 and cRNA promoter at 3.79 and 4.15 Å resolution, respectively, using cryo-EM (Fig. 3b, Extended Data Fig. 5a-h, Extended Data Table 2). The structure of the Nb8205-bound FluPol_A dimer is essentially identical to the dimer observed in the absence of Nb8205, showing the same binding mode for the 5' cRNA terminus with unresolved density around the template entry channel suggesting the presence of a dynamic 3' cRNA terminus in the active site (Extended Data Fig. 5i). In contrast, the structure of the Nb8205-bound FluPol_A monomer revealed the binding of both the 5' and 3' cRNA termini (Fig. 3b, Supplementary Video 1). The 5' cRNA terminus is bound in the hook conformation as observed in the FluPol_A dimer, while the 3' cRNA terminus occupies a binding site formed between the PA C-terminal domain and the PB1 thumb and PB2 N1 subdomains. Only bases 4 to 8 of the 15 nucleotide 3' cRNA could be resolved which are coordinated by residues of PB1 loop 553-571 and a series of charged residues of PA (E300, Y464, K488, R496) (Fig. 3c, Supplementary Video 1). We observed the same binding site for 3' cRNA in a cryo-EM structure of the monomeric form of influenza B virus polymerase (FluPol_B) (Extended Data Fig. 6a-f). This 3' cRNA binding site lies in close vicinity to the FluPol_A dimer interface (Extended Data Fig. 6g) and could represent a docking site for the 3' cRNA in the replication pre-initiation state of FluPol_A and could also accommodate the 3' cRNA during replication elongation, after it is copied and extruded through the template exit channel. This site is distinct from the previously observed 3' vRNA binding site in structures of bat FluPol_A and human FluPol_B but lies in a similar position as the 3' vRNA of the La Crosse orthobunyavirus RNA polymerase (Extended Data Fig. 6h)^{6,18,19}.

A comparison of the monomeric and dimeric FluPol_A structures in complex with Nb8205 revealed that dimerisation induces a movement of a helical bundle formed by the PB1 thumb and PB2 N1 subdomains (Fig. 3d, Supplementary Video 2). This movement results in an opening of the 3' cRNA binding site explaining the absence of 3' cRNA at this site in the dimeric structure. Furthermore, dimerisation leads to rearrangements in the polymerase active site that could destabilise the 3' cRNA binding, in agreement with the lack of density for the 3' extremity of the 3' cRNA in the dimer structure (Extended Data Fig. 5i). Specifically, the visible residues closest to the tip of the priming loop (PB1 residues E638 and M656) are moved away from the active site by approximately 7 Å, presumably pulling the tip out by a similar distance (Extended Data Fig. 6i, Supplementary Video 3). This movement of the priming loop and the destabilised binding of the 3' cRNA could facilitate backtracking of the cRNA template during the initiation of vRNA synthesis, in agreement with previous data that the priming loop is required during the realignment of the pppApG initiating dinucleotide to the cRNA terminus^{20,21}. In further support of this model we have solved the structure of FluPol_A bound to the vRNA promoter and capped RNA by cryo-EM at 3.0 Å resolution (Extended Data Fig. 7a-f). This structure, with the flexible PA endonuclease and PB2 C-terminal domains fully resolved, revealed the interaction of a fully resolved priming loop with the 3' vRNA in the active site (Extended Data Fig. 7g). The priming loop acts to buttress the template RNA positioning it next the catalytic aspartates (PB1 amino acid residues D445 and D446) to allow terminal initiation. This interaction is mediated by PB1 amino acid P651 at the tip of the priming loop that was found to be critical for priming loop function in our previous study²¹. The observed buttressing of the template by the priming loop is consistent with our proposed model for template realignment for vRNA synthesis triggered by polymerase dimerisation (Extended Data Fig. 7h, Supplementary Video 4).

To address the effect of Nb8205 on FluPol_A function, co-expression of Nb8205 in a minireplicon assay severely inhibited the accumulation of all viral RNAs, while another nanobody (Nb8210), also raised against FluPol_A but not affecting FluPol_A dimerisation (Extended Data Fig. 4a-c), had no significant effect (Fig. 4a). Nb8205 had no effect on capped RNA-primed transcription or cRNA synthesis on a vRNA template, but strongly inhibited vRNA synthesis on a cRNA template *in vitro* (Fig. 4b-d). Addition of Nb8205 to ApG dinucleotide-primed assays did not reduce activity but resulted in incorrectly initiated vRNA products on the cRNA template (Extended Data Fig. 8a-c). Nb8205 inhibited vRNA accumulation at 16 to 32 hours post-infection in cells infected with influenza A/WSN/33 virus and caused a significant reduction in virus titre, while Nb8210 had no or a much smaller effect (Fig. 4e).

Collectively, these data show that FluPol_A dimerisation is required for the initiation of vRNA synthesis on the cRNA template during viral genome replication (Fig. 4f). Replication initiation on the cRNA template being dependent on dimerisation is consistent with our previous observations that vRNA synthesis requires a trans-activating polymerase⁸. A requirement for trans-activation through polymerase dimerisation provides an elegant mechanism for tuning the amount of vRNA synthesised - only once there is a sufficient level of newly-made free polymerase available in the cell is vRNA production initiated. This could help ensure that the virus does not produce vRNA that cannot be assembled into

vRNPs and therefore could trigger an antiviral response through recognition by pathogen recognition receptors, e.g. RIG-I^{22,23}. It is interesting to note that numerous avian to mammalian adaptive mutations have been observed at the dimer interface suggesting that dimerisation of FluPol_A may be regulated in a host-specific manner (Extended Data Fig. 8d). In conclusion, the complete high-resolution structures of medically relevant human and avian FluPol_A and the identification of novel sites involved in polymerase dimerisation and cRNA promoter binding will provide guidance for the development of influenza antivirals.

Methods

Cells

Human embryonic kidney 293T (HEK-293T) and Sf9 insect cells were sourced from the Cell Bank of the Sir William Dunn School of Pathology, University of Oxford. HEK-293T cells were maintained in Dulbecco's Modified Eagle Medium (DMEM) and Sf9 cells were maintained in Sf-900 II serum free medium (Gibco). Cell lines have not been authenticated but tested negative for mycoplasma contamination.

Protein expression and purification

The three subunits of human influenza A/NT/60/1968 (H3N2) and avian influenza A/duck/Fujian/01/2002 (H5N1) virus polymerases were co-expressed in Sf9 cells from codon-optimized genes (GeneArt) cloned into a single baculovirus using the MultiBac system²⁴. Mutagenesis of H3N2 FluPol_A was carried out using the QuickChange Primer Design Program (Agilent). The influenza B/Panama/45/90 polymerase subunits were expressed as for FluPol_A, however they were cloned into the biGBac system²⁵ prior to bacmid generation. Expression and purification of wild-type and mutant FluPol_A and FluPol_B were performed as described⁸ with minor modifications. Size exclusion chromatography (SEC) was performed using 25 mM HEPES-NaOH, pH 7.5, 500 mM NaCl, and 5% (v/v) glycerol (Buffer A) on a Superdex 200 Increase 10/300 GL column (GE Healthcare). Pooled fractions from SEC were supplemented with 1 mM TCEP and the final product was concentrated to 3-5 mg ml⁻¹ and used for crystallisation or flash-frozen in liquid nitrogen and stored at -80 °C until further use. All purification steps were performed at 4 °C.

Generation, expression and purification of nanobodies

Nanobodies targeting H5N1 FluPol_A were generated following established protocols²⁶. Plasmids pMESy4 encoding C-terminal His₆-tagged nanobodies were transformed into *E. coli* strain WK6, grown in 2x YT medium containing 0.1% glucose, 2 mM MgCl₂ and 100 mg ml⁻¹ ampicillin at 37 °C until the A₆₀₀ of the sample reached 0.7, and then induced with 1 mM IPTG and incubated overnight at 28 °C. Cells were collected and the periplasmic fraction was extracted using the modified osmotic shock protocol. The periplasmic extract containing nanobody was incubated with Ni-NTA agarose (Qiagen) for 1 h at room temperature. The beads were washed with 20 volumes of 50 mM K₂HPO₄:NaH₂PO₄, pH 7.0, 1 M NaCl, followed by 30 volumes of 50 mM K₂HPO₄:NaH₂PO₄, pH 6.0, 1 M NaCl. Nanobodies were eluted by the addition of 15 volumes of 50 mM Na-acetate, pH 4.6, 1 M NaCl. The eluate was neutralised by the addition of 5 volumes of 1 M Tris-HCl, pH 7.5 and concentrated using an Amicon Ultra centrifugal filter unit (Merck Millipore). Nanobodies

were further purified on a Superdex 200 Increase 10/300 gel filtration column (GE Healthcare) in 20 mM Tris-HCl, pH 7.5, 150 mM NaCl. Nanobodies were concentrated to 4 mg ml⁻¹, flash-frozen and stored at -20 °C.

Crystallisation, data collection and structure determination

Initial hits were found in sitting-drop vapour-diffusion experiments²⁷ at 20 °C in conditions with 0.8-1.2 M phosphate buffer. After optimisation, H3N2 FluPol_A protein was crystallised in the condition of 0.9-1.2 M K₂HPO₄/NaH₂PO₄, pH 6.7, and H5N1 FluPol_A in the condition of 1 M K₂HPO₄/NaH₂PO₄, pH 6.9, 0.07% dichloromethane. Crystals appeared within 1-2 hours and grew to full size after 3-4 days. Crystals were cryo-protected by soaking for 10-30 seconds in 25% (v/v) glycerol or 20% (v/v) ethylene glycol in crystallisation buffer before flash-freezing in liquid nitrogen. H3N2 FluPol_A was co-crystallised with nanobody Nb8205, added to FluPol_A in a 1.5 fold molar excess, using the same conditions as for apo FluPol_A. Additional nanobody was added during crystal stabilisation and freezing. Diffraction data were collected at -173 °C on beamlines I03 (wavelength 0.9159 Å) and I24 (wavelength 0.9686 Å) (for H3N2 FluPol_A) and I04 (wavelength 0.9795 Å) (for H5N1 FluPol_A and H3N2 FluPol_A+Nb8205), at the Diamond Light Source, Didcot, UK. Data were processed using XDS²⁸ and STARANISO²⁹, using an anisotropic cut-off and the mean $I/\sigma(I)$ value of 1.20 to determine the diffraction-limit surface. The structure of H5N1 FluPol_A was solved by molecular replacement using Phaser-MR³⁰ as implemented in PHENIX³¹ and a search model of the FluPol_C structure¹⁵ (PDB ID: 5D98) with the PB2 627 domain deleted from the model. Phases of individual 627 domains were obtained by a second round of molecular replacement. After rigid-body refinement, the structure was rebuilt with COOT³² and refined with PHENIX³¹ and autoBUSTER³³ until R-factor values converged. Translation-libration-screw (TLS) parameters and 4-fold torsion-angle non-crystallographic symmetry (NCS) were also applied in refinement. The structure of H3N2 FluPol_A was solved by molecular replacement using the structure of H5N1 FluPol_A (this study) as the search model and refined in the same way. To determine the structure of human FluPol_A in complex with nanobody Nb8205, chain N of PDB ID: 3SN6³⁴ was used as a search model for the nanobody. In the final H3N2 FluPol_A model 93.31 % residues are in the most favoured regions of the Ramachandran plot and 0.09 % are in the disallowed regions (90.93 % and 0.08 % for H5N1 FluPol_A model, and 92.65 % and 0 % for H3N2 FluPol_A+Nb8205 model, respectively).

Cryo-EM sample preparation

Purified dimer fraction of H3N2 FluPol_A was mixed with a 1.2 fold molar excess of 5' and 3' cRNA promoters (5' cRNA: 5'-pAGCAAAGCAGGCC-3'; 3' cRNA: 5'-GGCCUUGUUUCUACU-3') or vRNA promoters (5' vRNA: 5'-pAGUAGAAACAAGGCC-3'; 3' vRNA: 5'-GGCCUGCUUUUGCU-3') and, if stated, a 2.5 fold molar excess of purified nanobody Nb8205 to prepare cRNA-bound FluPol_A-nanobody complex. The samples were injected on a Superdex 200 Increase 10/300 GL column (GE Healthcare) running in 25 mM HEPES-NaOH, pH 7.5, 500 mM NaCl. The fractions of interest were concentrated, and protein surface charges were neutralized by adding 0.001% glutaraldehyde for 20 min on ice in order to minimize preferential orientation of particles. After quenching the reaction by adding Tris-HCl, pH 8.0 to a final

concentration of 100 mM, the sample was re-injected on a Superdex 200 Increase 10/300 GL column (GE Healthcare) running in 25 mM HEPES-NaOH, pH 7.5, 500 mM NaCl. The fractions of interest were concentrated to 1 mg ml⁻¹ and diluted three fold into 25 mM HEPES-NaOH, pH 7.5, 37.5 mM NaSCN, 0.0075% (v/v) Tween 20 prior to grid preparation. A volume of 3.5 µl of cRNA-bound FluPol_A at a concentration of 0.35 mg ml⁻¹ was placed on glow discharged carbon-coated (40 nm film) copper C-flat grids (Protochips) with 2 µm holes and 1.0 µm spacing before blotting for 3.5 s and flash-freezing in liquid ethane. Purified dimer fraction of FluPol_B was mixed with a 1.2 fold molar excess of 5' and 3' cRNA promoters (5' cRNA: 5'-pAGCAAAGCAGGCC-3'; 3' cRNA: 5'-GGCCUUGUUUCUACU-3') and the sample was processed as described for FluPol_A and concentrated to 0.35 mg ml⁻¹. A volume of 3.5 µl of cRNA-bound FluPol_B was used to prepare grids as described above. All grids were prepared using a Vitrobot mark IV (FEI) at 95-100% humidity.

Cryo-EM image collection and processing

Cryo-EM data were collected on a 300 kV Titan Krios microscope (Thermo Fisher Scientific) fitted with a GIF Quantum energy filter (Gatan) at either the Division of Structural Biology (Strubi) or Electron Bio-Imaging Centre (eBIC). For the FluPol_A data sets a Volta Phase Plate (Thermo Fisher Scientific) was used. Micrographs were recorded in counting mode using a K2 Summit (Gatan) direct electron detector (or K3 for the FluPol_A-vRNA dataset). For sample-specific data collection parameters, see Extended Data Table 2. Movie data were processed using MotionCor2-1.1.0³⁵, with a 5 by 5 patch-based alignment, keeping all the frames and dose weighting up to the total exposure. The contrast transfer function and additional phase-shift of full dose non-weighted micrographs was estimated using Gctf-v1.18 or Gctf-v1.06³⁶ for the FluPol_B dataset. Poor-quality images were discarded after manual inspection. For cRNA-bound dimeric FluPol_A, 56,070 particles were manually picked from the dose-weighted micrographs using the RELION 3.0³⁷ manual picking tool, then extracted in a 250 pixel box and subjected to one round of 2D classification resulting in 16 classes with 43,316 selected particles. 3D classification with alignment into three different classes was performed. Two of the classes containing a total number of 36,913 particles were selected and refined to 4.2 Å with C2 symmetry. Bayesian polishing and per particle CTF refinement were performed in RELION 3.0 improving map resolution up to 4.07 Å. The same particles were also refined without symmetry resulting in a map with a resolution of 4.34 Å. Local resolution estimation and sharpening was performed by the RELION sharpening tool using a -100 Å² and -80 Å² B-factor, respectively. For the cRNA-bound FluPol_A-Nb8205 complex, a first of set of 406,945 particles has been automatically picked with the template picker implemented in cryoSPARC v2.5³⁸ using 2D classes from cRNA-bound FluPol_A as a template and then 2D classified. A final set of 34,162 particles containing only the dimeric form of the complex has been exported to RELION 3.0 in a 250 pixel box while the monomeric classes have been used as template for another round of automatic picking. From an initial set of 505,860 particles, 216,066 particles containing only the monomeric form were selected after 2D classification and exported into RELION 3.0 in a 200 pixel box. Both dimer and monomer data sets were refined individually to a resolution at 4.38 Å and 4.1 Å using C1 symmetry, respectively. Bayesian polishing and per particle CTF refinement were performed in

RELION 3.0 improving map resolution up to 4.15 Å and 3.79 Å, respectively. For the vRNA-bound FluPol_A, a first of set of 2,210,168 particles has been automatically picked with the template picker implemented in cryoSPARC v2.5³⁸ using 2D classes from cRNA-bound FluPol_A as a template and then 2D classified. A final set of 432,160 particles containing only the monomeric form of the complex has been exported to RELION 3.0 in a 250 pixel box. The data were refined to a resolution at 3.3 Å using C1 symmetry. Bayesian polishing and per particle CTF refinement were performed in RELION 3.0 improving map resolution up to 2.9 Å. A final iteration of 3D classification was performed in RELION 3.0, giving a final map at a resolution of 3.01 Å with a final set of 170,144 particles. For cRNA-bound FluPol_B, a first of set of 1,012,085 particles was automatically picked with the template picker implemented in cryoSPARC v2.5³⁸ using 2D classes of the cRNA-bound FluPol_A-Nb8205 complex as a template. After 2D classification, the best views were selected for another round of automatic picking. From an initial set of 324,395 particles, 41,549 particles were selected after 3D classification and exported to RELION 3.0 in a 200 pixel box. The data were refined to a resolution at 4.18 Å using C1 symmetry. The structures were modelled by first fitting an initial model into the locally sharpened map using UCSF Chimera³⁹. One cycle of rigid body real space refinement followed by manual adjustment in Coot⁴⁰ was performed to correctly position the C α chain into the density. Finally, cycles of PHENIX³¹ real space refinement and manual building in Coot⁴⁰ were used to improve model geometry. Map-to-model comparison in PHENIX mtriage validated that no over-fitting was present in the structures. Model geometry was validated for all models using MolProbity⁴¹. All map and model statistics are detailed in Extended Data Table S2.

Analytical size-exclusion chromatography (SEC)

Analytical SEC experiments were performed on a Superdex 200 Increase 10/300 GL column (GE Healthcare) using Buffer A. Wild-type or mutant FluPol_A were loaded via a 100 μ l sample loop at a concentration of 10 μ M. For investigating the effect of nanobodies, the nanobody was added to FluPol_A in a 1.5 fold molar excess and incubated on ice for one hour before injection.

Size-exclusion chromatography coupled small-angle X-ray scattering (SEC-SAXS)

SEC-SAXS experiments were performed on beamline B21 at the Diamond Light Source, Didcot, UK. 45 μ l purified FluPol_A at a concentration of 12 μ M was injected on a Shodex KW-403 size exclusion column under a flow rate of 0.16 ml min⁻¹ at 20°C in Buffer A. Data were collected using continuous 3 second exposures. The data were buffer-subtracted, scaled, merged, and analysed using the ScÅtter 3.0 software (<http://www.bioisis.net/scatter>). Molecular weight of each individual frame was estimated from DATASW⁴².

Size-exclusion chromatography coupled multi-angle light scattering (SEC-MALS)

SEC-MALS experiments were performed on beamline B21 at the Diamond Light Source, Didcot, UK. 45 μ l purified FluPol_A at a concentration of 4 μ M was injected on a Shodex KW-403 size exclusion column under a flow rate of 0.16 ml min⁻¹ at 20°C in Buffer A in the absence of glycerol. An 18-angle multi-angle light scattering instrument (DAWN HELEOS, WYATT) was used to collect light scattering data and the data were processed with ASTRA (WYATT).

Plasmids

Plasmids pcDNA-PB1, pcDNA-PB1a, pcDNA-PB1-FLAG, pcDNA-PB1-TAP (PB1 fused to a C-terminal tandem affinity purification [TAP] tag that consists of a calmodulin binding domain [CBD], a tobacco etch virus [TEV] protease cleavage site, and two copies of protein A), pcDNA-PB2, pcDNA-PB2-TAP, pcDNA-PA, pcDNA-PA_{D108A}, pcDNA-NP and pPOLI-NA have been described^{12,43–47}. Plasmids pcDNA-PB2_{71–73A}, pcDNA-PA_{351–353A}, pcDNA-PA_{356–358A}, and pcDNA-PA_{352–356A}, encoding mutant PB2 and PA polymerase subunits, were generated from pcDNA-PB2 and pcDNA-PA using site-directed PCR mutagenesis. Plasmids pcDNA-Nb8205 and pcDNA-Nb8210, to express nanobodies Nb8205 and Nb8210 in mammalian cells, were generated by PCR amplification using pMESy4 plasmids as templates and cloning into pcDNA3A.

FluPol_A dimerisation assay

Dimerisation of FluPol_A in human embryonic kidney 293T (HEK-293T) cells was assessed as described⁴⁸. Protein complexes were analysed by SDS-PAGE and silver staining using SilverXpress (Invitrogen) and bands of PB1-FLAG and PB1-CBD quantitated in ImageJ⁴⁹.

RNP reconstitution assay and primer extension analysis

Approximately 0.2×10^6 HEK-293T cells were transfected with 0.2 μ g of each pcDNA plasmid encoding PB1, PB2, PA, NP and pPOLI plasmid encoding neuraminidase (NA) vRNA segment, using Lipofectamine 2000 (Invitrogen) according to the manufacturer's instructions. Plasmids encoding mutant proteins or nanobodies were included as indicated. For the complementation assay with a transcription-deficient but replication-competent PA_{D108A} polymerase equal amounts of pcDNA-PA_{D108A} and pcDNA-PA_{356–358A} were co-transfected as described previously^{13,48}. Cells were harvested 20 hours post-transfection and total cellular RNA was extracted using TRI reagent (Sigma) according to the manufacturer's instructions. Viral RNA levels were analysed using primer extension as described⁵⁰. Briefly, RNA was reverse transcribed using ³²P-labelled primers specific to positive and negative sense viral RNAs, with a primer specific to cellular 5S rRNA as a loading control. Transcripts were separated by 6% denaturing PAGE and visualised by phosphorimaging on an FLA-5000 scanner (Fuji). Analysis was carried out using ImageJ⁴⁹ and Prism 7 (GraphPad). Viral RNA levels were normalised to the 5S rRNA loading control.

Virus growth analysis

Approximately 10^6 HEK-293T cells were transfected with 5 μ g of pcDNA plasmid encoding Nb8205, Nb8210, or an empty pcDNA3 vector using Lipofectamine 2000 (Invitrogen) according to the manufacturer's instructions. 24 hours post-transfection, cells were infected with influenza A/WSN/33 virus at an MOI 0.1. Media was collected 12, 24, 36 and 48 hours post-infection, and virus titres were determined by plaque assay. At each time point, total cellular RNA was also extracted using TRI reagent (Sigma) and vRNA levels were analysed by primer extension⁵⁰.

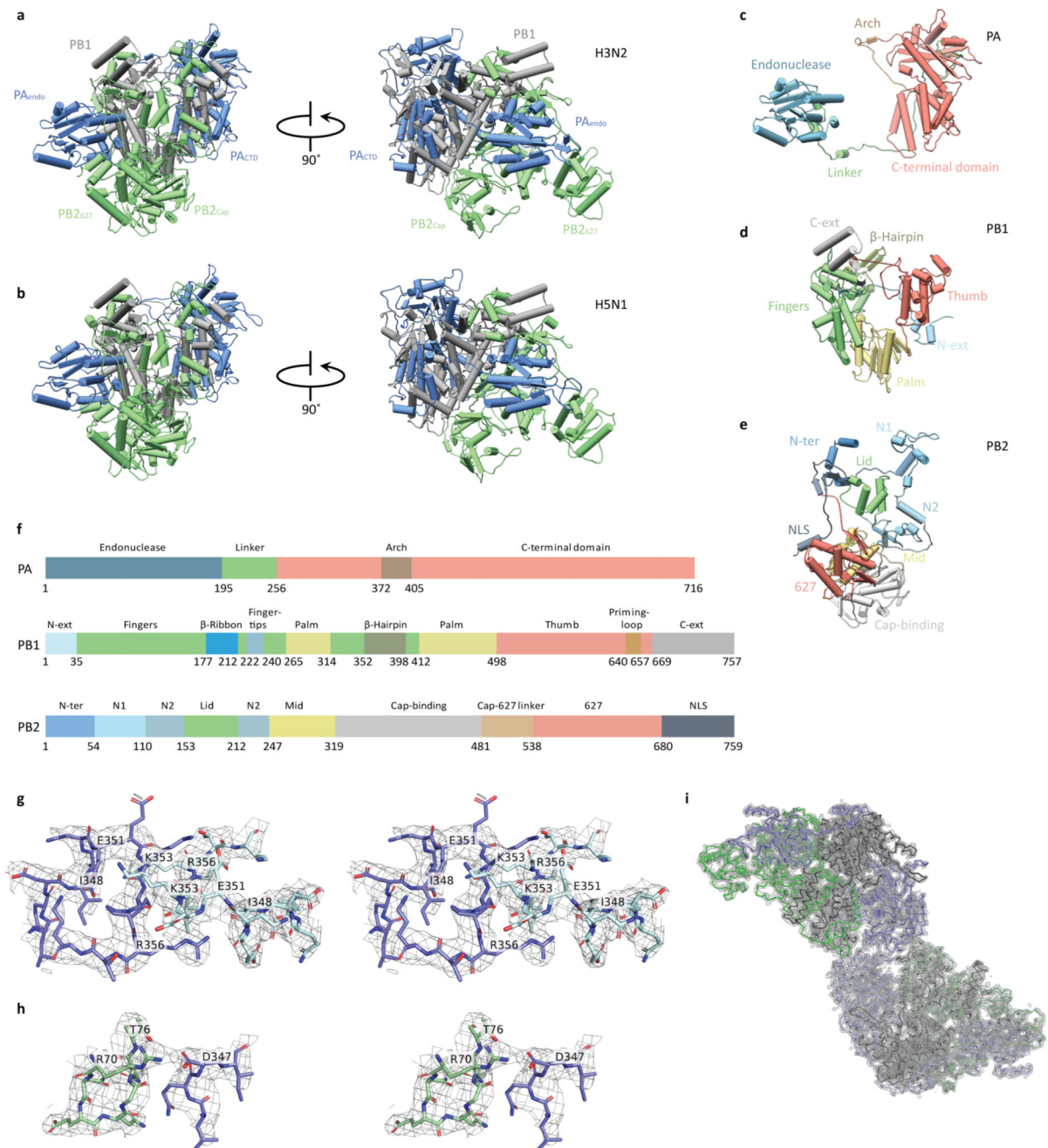
***In vitro* transcription assays**

In vitro transcription assays were carried out as described²¹. Briefly, a cap-1 structure was added to a synthetic 11-nucleotide RNA (5'-ppGAAUACUCAAG-3') (ChemGenes) by mixing 1 μM of RNA with 0.25 μM [α -³²P]GTP (3000 Ci mmol⁻¹; Perkin-Elmer), 0.8 mM S-adenosylmethionine, 0.5 U μl^{-1} vaccinia virus capping enzyme (NEB) and 2.5 U μl^{-1} 2'-O-methyltransferase (NEB) in a 20 μl reaction at 37 °C for 1 hour. The product was isolated by 16% denaturing PAGE, excised, eluted overnight in dH₂O, and desalted using NAP-10 columns (GE Healthcare). Transcription reactions were performed using ~1,500 c.p.m. capped RNA primer in a 3 μl reaction mixture containing 1mM ATP, 0.5 mM CTP, 0.5 mM UTP, 0.1 μM GTP, 5 mM MgCl₂, 1 mM DTT, 2 U μl^{-1} RNasin, 0.5 μM 5' vRNA promoter, 0.5 μM 3' vRNA promoter, 70 ng Nb8205 (if indicated) and 100 ng H3N2 FluPol_A. Reactions were incubated for 10 min at 30 °C and stopped by the addition of an equal volume of 80% formamide, 1 mM EDTA, and bromophenol blue and xylene cyanol dyes, followed by incubation at 95 °C for 3 min. Products were resolved by 20% denaturing PAGE and visualised by phosphorimaging on an FLA-5000 scanner (Fuji). Analysis was carried out using ImageJ⁴⁹ and Prism 7 (GraphPad).

***In vitro* replication assays**

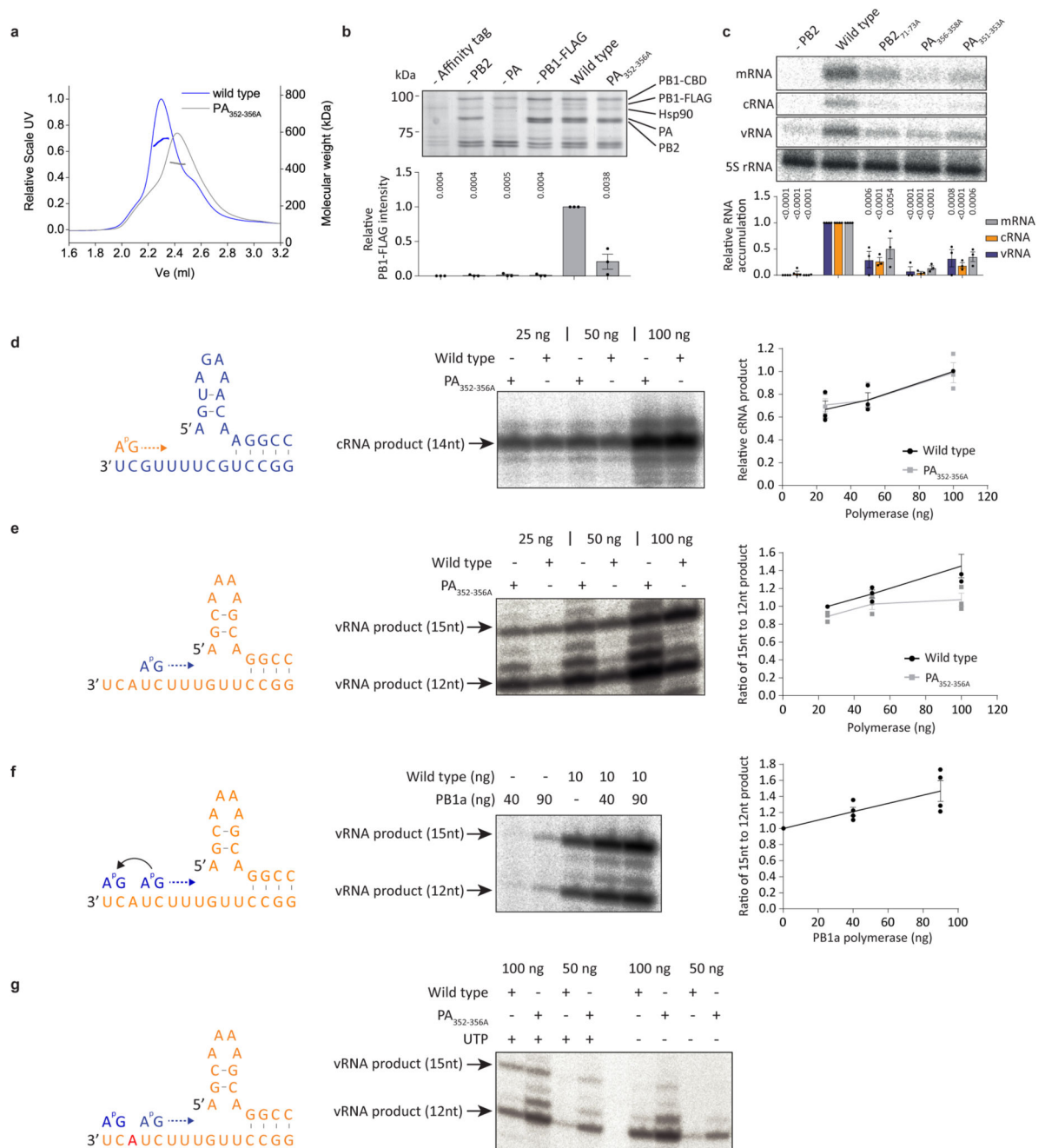
Primer-independent and ApG extension assays were carried out as described²¹. Briefly, 3 μl reaction mixtures containing 1 mM ATP, 0.5 mM CTP, 0.5 mM UTP (if indicated), 0.1 μM GTP, 0.05 μM [α -³²P]GTP (3000 Ci mmol⁻¹; Perkin-Elmer), 0.25 mM ApG (if indicated), 5 mM MgCl₂, 1 mM DTT, 2 U μl^{-1} RNasin, 0.5 μM 5' vRNA or cRNA promoter, 0.5 μM 3' vRNA or cRNA promoter, 70 ng Nb8205 (if indicated) and 10-100 ng H3N2 FluPol_A were incubated at 37 °C for 4 hours. Where PB1a active site mutant polymerase was added, the concentrations of 5' and 3' cRNA promoters were adjusted accordingly to maintain a constant molar ratio of promoter to polymerase. Reactions were stopped by addition of an equal volume of 80% formamide, 1 mM EDTA, and bromophenol blue and xylene cyanol dyes, followed by incubation at 95 °C for 3 min. Products were resolved by 20% denaturing PAGE and visualised by phosphorimaging on an FLA-5000 scanner (Fuji). Analysis was carried out using imageJ⁴⁹ and Prism 7 (GraphPad).

Extended Data

**Extended Data Fig. 1. Subunit organisation of FluPol_A heterotrimers.**

a, b, Views of the structure of human H3N2 (**a**) and avian H5N1 (**b**) FluPol_A heterotrimers, coloured according to subunit. **c–e**, Structures of human H3N2 FluPol_A subunits PA (**c**), PB1 (**d**) and PB2 (**e**), coloured and labelled by domain. **f**, Domain maps of each H3N2 FluPol_A subunit. **g–i**, The 2D $F_o - mF_c$ electron density maps of FluPol_A dimer interface as shown in Fig. 1c (**g**, stereo view), and 1d (**h**, stereo view), as well as of the complete FluPol_A dimer

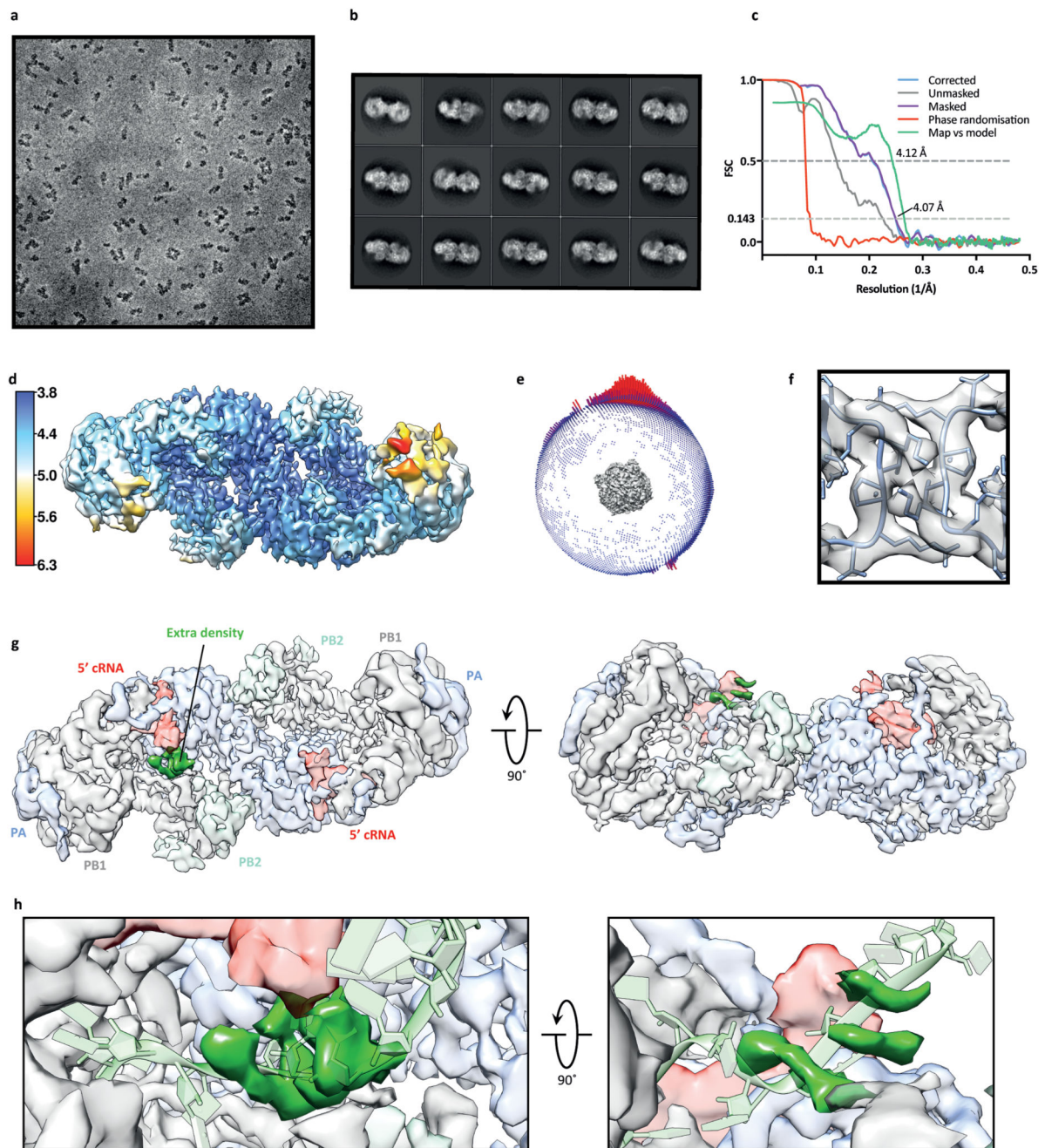
(i), are shown in gray mesh (contoured at 1.5σ , all from the H3N2 FluPol_A structure model).



Extended Data Fig. 2. Effect of mutations at the dimer interface on FluPol_A dimerisation and activity.

a, SEC-MALS analysis of wild type and PA_{352-356A} mutant H3N2 FluPol_A (n=1 independent experiment). Smooth lines reflect the relative UV signal of SEC and dotted lines indicate estimated molecular weight for each frame. Note that monomeric FluPol_A heterotrimer has an approximate molecular weight of 255 kDa. **b**, Effect of PA_{352-356A}

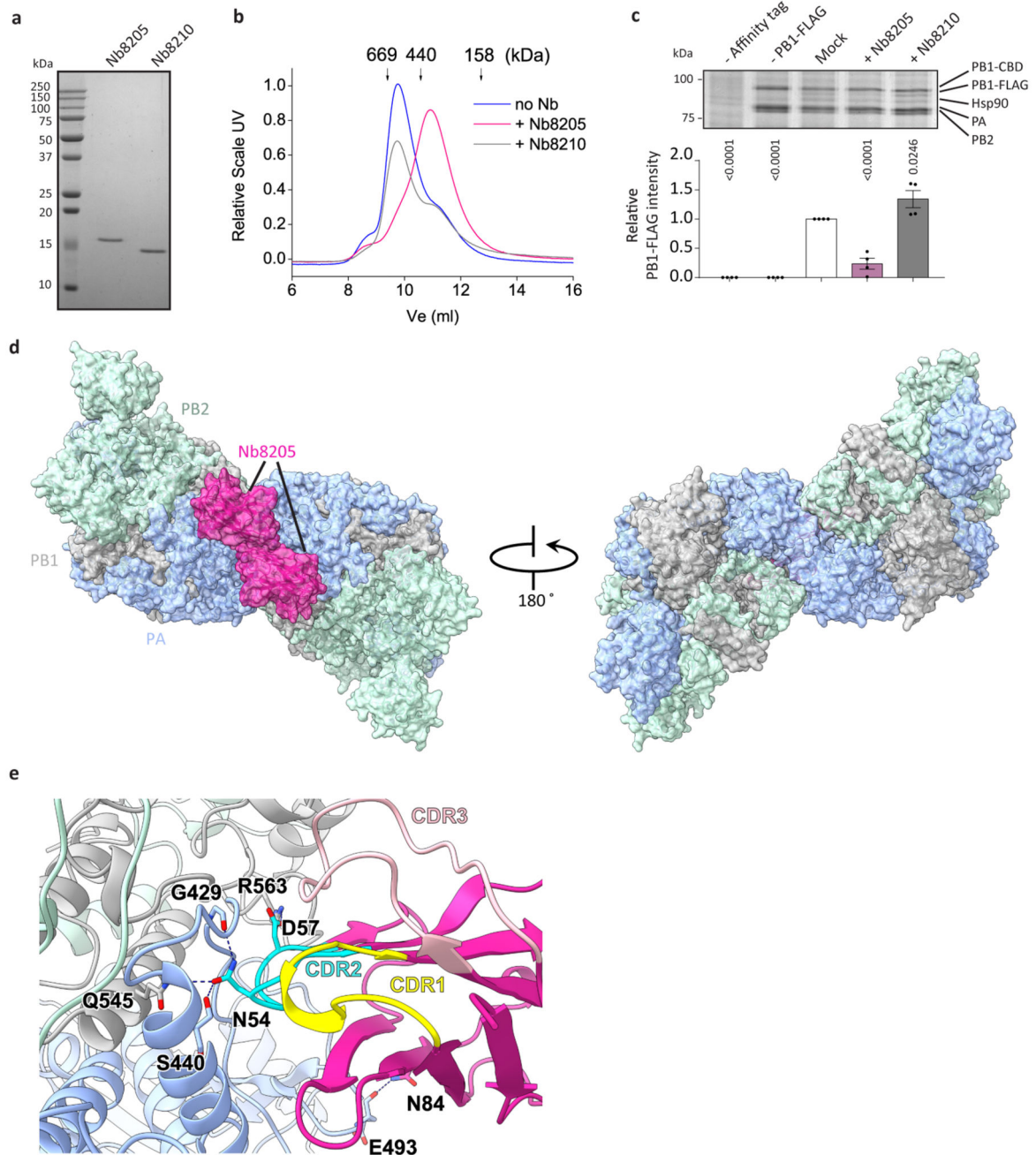
mutation on FluPol_A dimerisation in HEK-293T cells. Data are mean \pm s.e.m., n=3 independent transfections. One-way ANOVA. $P < 0.05$ is considered significant. **c**, Effect of mutations designed to destabilise PB2 and PA loops at the FluPol_A dimer interface on FluPol_A activity in a vRNP reconstitution assay. Data are mean \pm s.e.m., n=3 independent transfections. Two-way ANOVA. $P < 0.05$ is considered significant. **d, e**, Effect of PA_{352-356A} mutation on *in vitro* ApG-primer replication by FluPol_A on a vRNA (**d**) and cRNA (**e**) template. **f**, Effect of an active site polymerase mutant (PB1a) on *in vitro* ApG-primer replication by FluPol_A on a cRNA template. Data are mean \pm s.e.m., n=4 independent reactions. **g**, Omitting UTP from *in vitro* ApG-primer replication by FluPol_A on a cRNA template affects the synthesis of the 15 nucleotide full-length vRNA but not of the 12 nucleotide short vRNA indicating that the 12 nucleotide product is derived from internal initiation by the ApG dinucleotide at positions 4 and 5 of the cRNA template. The position in the template at which UTP is required is indicated in red. Representative data from n=2 independent reactions. For gel source data, see Supplementary Fig. 2.



Extended Data Fig. 3. Single-particle cryo-EM analysis of human H3N2 FluPol_A bound to cRNA promoter.

a, Representative micrograph of cRNA-bound FluPol_A heterotrimer particles embedded in vitreous ice. **b**, Representative 2D class averages. **c**, FSC curves for 3D reconstruction using gold-standard refinement in RELION, indicating overall map resolution of 4.07 Å and the model-to-map FSC. Curves are shown for phase randomisation, unmasked, masked and phase-randomisation-corrected masked maps. **d**, 3D reconstruction locally filtered and coloured according to RELION local resolution. **e**, Angular distribution of particle

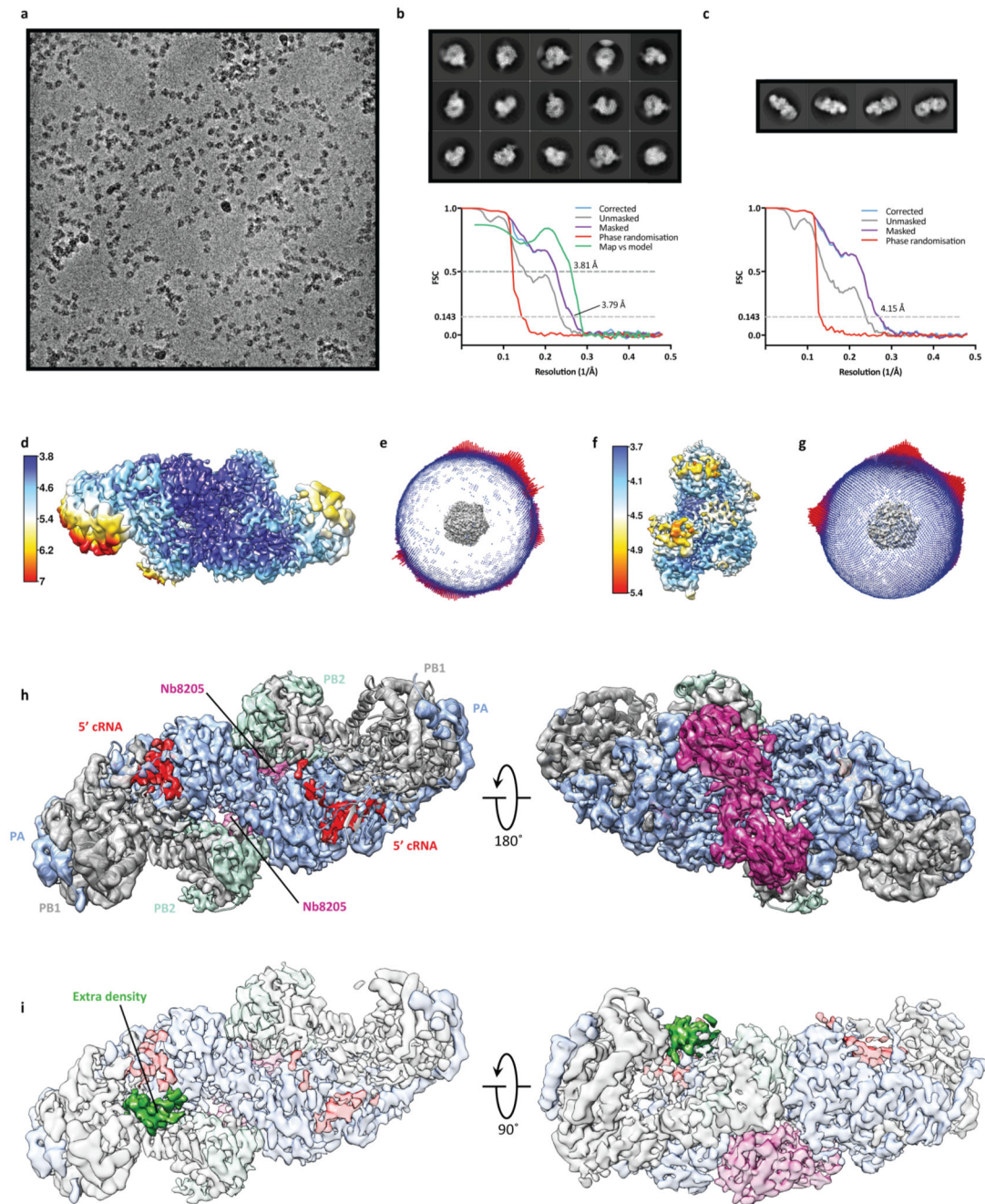
projections with the cryo-EM map shown in grey. **f**, Cryo-EM density of the PA loop 352-356 at the dimer interface. **g**, Cryo-EM map of cRNA-bound FluPol_A dimer refined without symmetry imposed (C1), revealing an extra density (green) located next to the 3' end of the 5' cRNA close to the template entry channel. **h**, Close-up views highlighting cryo-EM extra density (dark green) with the 3' vRNA strand from the superimposed FluPol_B structure⁵¹ (PDB: 5MSG, light green) inserting into the polymerase active site. Localisation of the 3' vRNA shows that bases are positioned in the extra density facing the density corresponding to the 3' end of the 5' cRNA, suggesting the presence of a promoter RNA duplex region as observed in vRNA-bound FluPol_B⁵¹. The extra density is consistent with the presence of a 3' cRNA in one of the heterotrimers of the cRNA-bound FluPol_A dimer, oriented towards the polymerase active site.



Extended Data Fig. 4. The effect of Nb8205 on FluPol_A dimerisation.

a, SDS-PAGE of purified nanobodies ($n=1$ independent experiment). **B**, Analytical SEC of FluPol_A in complex with nanobodies ($n=4$ for Nb8205 and $n=2$ for Nb8210, with similar results). **c**, Effect of nanobodies on FluPol_A dimerisation in HEK-293T cells. Data are mean \pm s.e.m., $n=4$ independent transfections. One-way ANOVA. $P < 0.05$ is considered significant. For gel source data, see Supplementary Fig. 2. **d**, Crystal structure of H3N2 FluPol_A in complex with Nb8205. **e**, Close-up view of FluPol_A-Nb8205 interactions. Residues involved in hydrogen bonding interactions are labelled and hydrogen bonds are

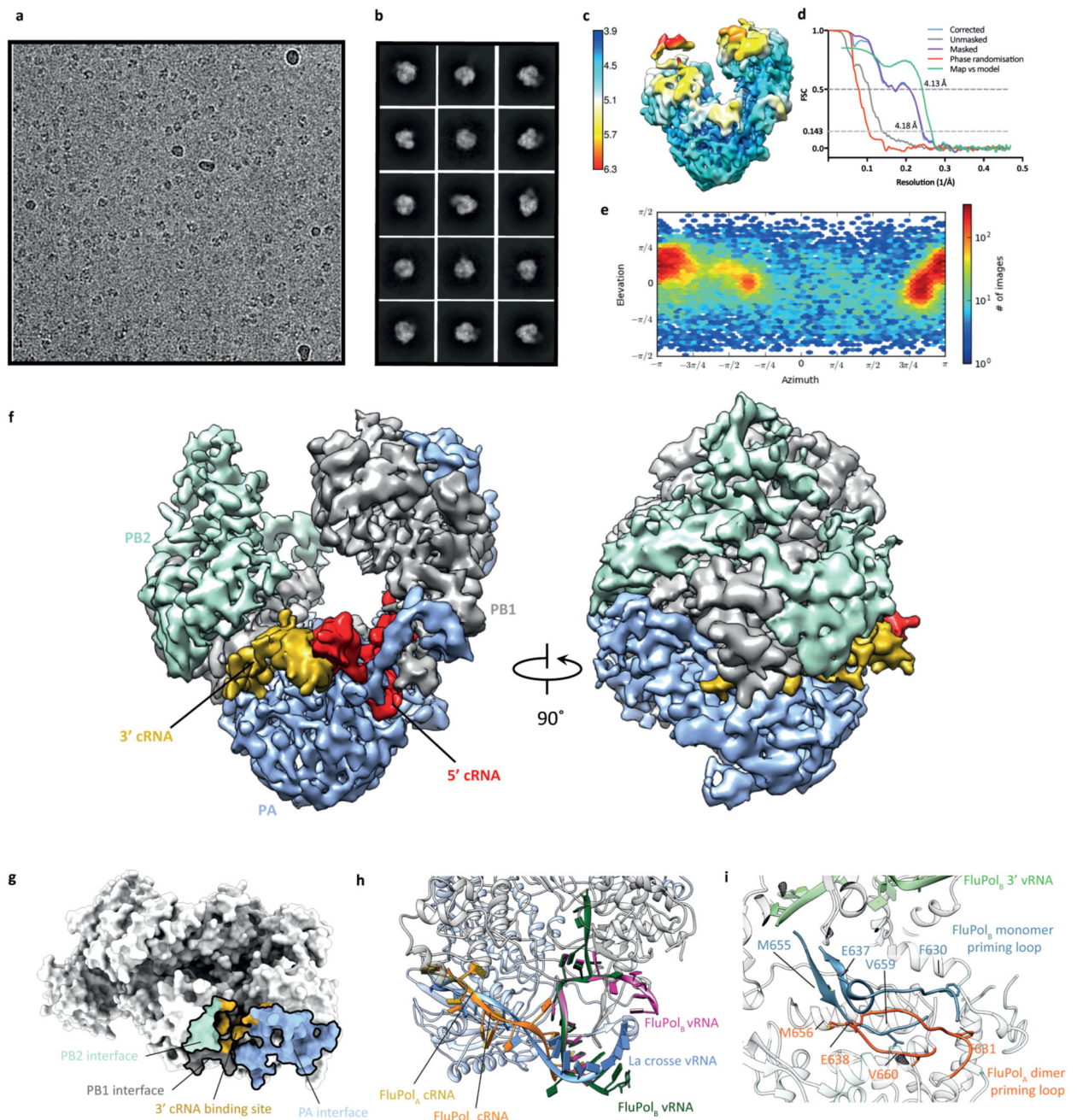
indicated with dashed lines. The complementarity determining regions (CDRs) are coloured individually and labelled.



Extended Data Fig. 5. Single-particle cryo-EM analysis of monomeric and dimeric cRNA-bound human H3N2 FluPol_A heterotrimer in complex with Nb8205.

a, Representative micrograph of cRNA-bound FluPol_A in complex with Nb8205 embedded in vitreous ice. **b**, Representative 2D class averages. **c**, FSC curves for the 3D reconstruction using gold-standard refinement in RELION, indicating overall map resolution of 3.79 Å and 4.15 Å for the monomeric and dimeric FluPol_A form, respectively, and the model-to-map

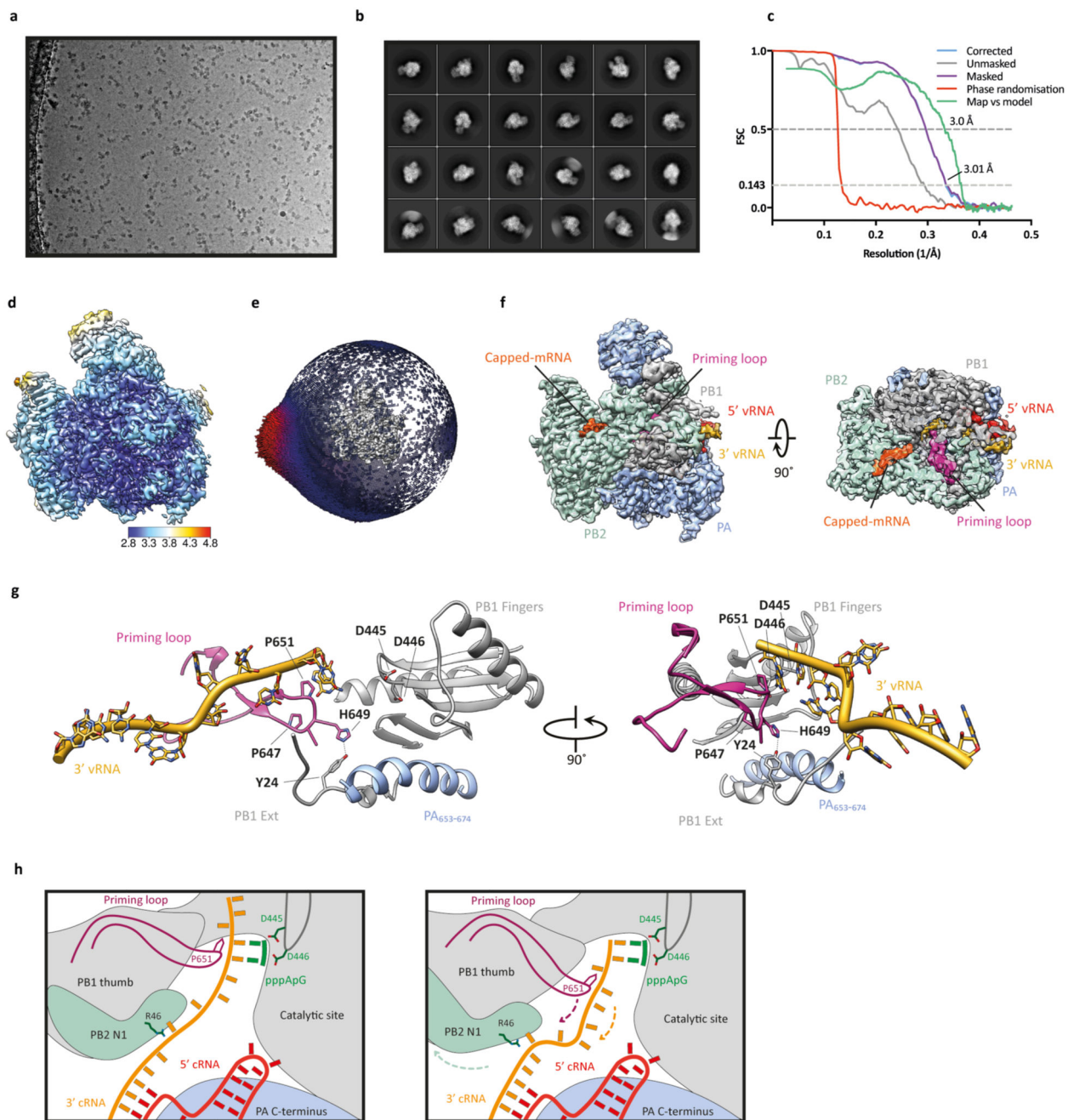
FSC. Curves are shown for phase randomisation, unmasked, masked and phase-randomisation-corrected masked maps. **d, f**, 3D reconstruction locally filtered and coloured according to RELION local resolution for the dimeric (**d**) and monomeric (**f**) form. **e, g**, Angular distribution of particle projections for the dimeric (**e**) and monomeric (**g**) form with the cryo-EM map shown in grey. **h**, Dimer of FluPol_A heterotrimers bound to cRNA promoter and Nb8205 rigid body fitted into the cryo-EM map of dimeric cRNA-bound FluPol_A heterotrimer in complex with Nb8205. **i**, Cryo-EM map of the dimeric cRNA-bound FluPol_A heterotrimer in complex with Nb8205 revealing an extra density (green) located next to the 3' end of the 5' cRNA, as observed for the cRNA-bound FluPol_A dimer (Extended Data Fig. 3g, h).



Extended Data Fig. 6. Single-particle cryo-EM analysis of cRNA-bound FluPol_B.

a, Representative micrograph of cRNA-bound FluPol_B heterotrimer particles embedded in vitreous ice **b**, Representative 2D class averages. **c**, 3D reconstruction locally filtered and coloured according to RELION local resolution. **d**, FSC curves for the 3D reconstruction using gold-standard refinement in RELION, indicating overall map resolution of 4.18 Å and the model-to-map FSC. Curves are shown for the phase randomisation, unmasked, masked, phase-randomisation-corrected masked maps. **e**, Angular distribution of particle projections according to cryoSPARC v2.5 non-uniform refinement. **f**, Cryo-EM map of cRNA-bound

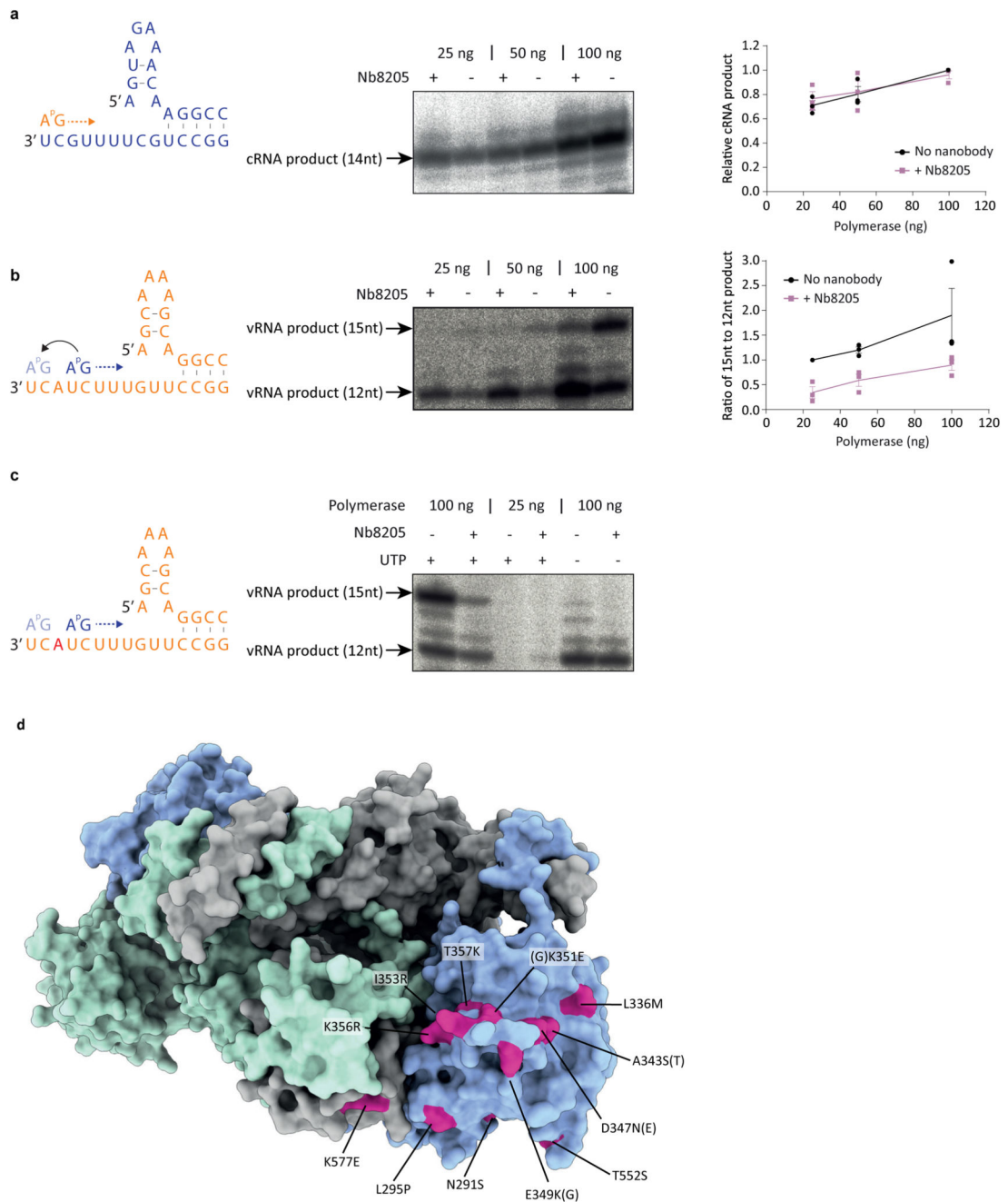
FluPol_B. **g**, Comparison of the dimerisation interface and the 3' cRNA binding site in H3N2 FluPol_A (PDB: 6QNW and 6QPG). **h**, 3' cRNA binding site in FluPol_A and FluPol_B overlaps with the previously identified 3' vRNA binding site in the La Crosse orthobunyavirus polymerase¹⁹ (PDB: 5AMQ). Sites of 3' vRNA binding at surface of the polymerase in FluPol_B (PDB: 4WRT) and in the polymerase active site for FluPol_B (PDB: 5MSG) are shown for comparison^{6,51}. **i**, Comparison of the structure of dimeric FluPol_A to monomeric FluPol_B⁵¹ (PDB: 5MSG) reveals a movement of the priming loop that protrudes from the PB1 thumb subdomain into the polymerase active site. Resolved PB1 residues closest to the tip of the priming loop, E638 and M656, move away from the corresponding E637 and M655 residues in FluPol_B and the polymerase active site, indicated by the end of the 3' vRNA, by approximately 7 Å.



Extended Data Fig. 7. Single-particle cryo-EM analysis of human H3N2 FluPol_A bound to vRNA promoter.

a, Representative micrograph of vRNA-bound FluPol_A heterotrimer particles embedded in vitreous ice. **b**, Representative 2D class averages. **c**, FSC curves for 3D reconstruction using gold-standard refinement in RELION, indicating overall map resolution of 3.01 Å and the model-to-map FSC. Curves are shown for phase randomisation, unmasked, masked and phase-randomisation-corrected masked maps. **d**, 3D reconstruction locally filtered and coloured according to RELION local resolution. **e**, Angular distribution of particle

projections with the cryo-EM map shown in grey. **f**, Cryo-EM map of vRNA-bound FluPol_A heterotrimer revealing the presence of a fully resolved priming loop. **g**, Close-up views highlighting the stacking of the 3' vRNA by the priming loop. **h**, Cartoon illustration of the role of polymerase dimerisation in template realignment during replication initiation on a cRNA template. Base-pairing between the 5' and 3' cRNA positions bases 4 and 5 of the 3' cRNA next to the catalytic aspartates (PB1 amino acid residues D445 and D446) in the active site to allow internal replication initiation by the synthesis of a pppApG dinucleotide. The priming loop stacks the cRNA template through PB1 amino acid P651 (left panel). Rotation of the PB1 thumb/PB2-N1 domain triggered by polymerase dimerisation results in a movement of the priming loop and backtracking of the stacked template (arrows). Backtracking is also facilitated by an interaction of PB2 amino acid residue R46 with the 3' cRNA introducing a 'kink' in the template. Backtracking positions bases 1 and 2 of the cRNA template opposite the pppApG dinucleotide that remains coordinated by the catalytic aspartates. The resulting replication complex is ready to extend the pppApG dinucleotide by incorporating the next incoming NTP (right panel).



Extended Data Fig. 8. Effect of Nb8205 on FluPol_A activity and mapping of host adaptive mutations at the FluPol_A dimer interface.

a, b, Effect of Nb8205 on *in vitro* ApG-primer replication by FluPol_A on a vRNA (**a**) and cRNA (**b**) template. Data are mean \pm s.e.m., $n=3$ independent reactions. **c**, Omitting UTP from *in vitro* ApG-primer replication by FluPol_A on a cRNA template affects the synthesis of the 15 nucleotide full-length vRNA but not of the 12 nucleotide short vRNA. The position in the template at which UTP is required is indicated in red. Representative data from $n=2$ independent reactions. For gel source data, see Supplementary Fig. 2. **d**, Crystal structure of

H3N2 FluPol_A with amino acid residues implicated in avian to mammalian host adaptation of influenza A viruses indicated^{52–66}.

Extended Table 1
Crystallographic data collection and refinement statistics

	H3N2 FluPol _A PDB: 6QNW	HSN1 FluPol _A PDB: 6QPF	H3N2 FluPol _A -Nb8205 PDB: 6QPG
Data collection			
Space group	C2	C2	C2
Cell dimensions			
<i>a, b, c</i> (Å)	336.5, 191.9, 235.7	337.1, 192.9, 235.7	335.2, 192.9, 235.1
α, β, γ (°)	90.0, 91.5, 90.0	90.0, 91.5, 90.0	90.0, 91.8, 90.0
Resolution* (Å)	235.6-3.3 (3.92-3.32)	235.6-3.6 (4.27-3.63)	235.0-3.3 (3.87-3.34)
<i>R</i> _{merge} * (ellipsoidal)	0.46 (2.24)	0.18 (0.61)	0.34 (1.24)
<i>I</i> / σ <i>I</i> *	4.8 (2.0)	2.9 (1.6)	4.8 (1.8)
Completeness* (% , ellipsoidal)	95.3 (80.7)	92.7 (72.4)	91.9 (74.5)
Redundancy*	14.4 (13.7)	3.4 (3.4)	7.0 (6.9)
Refinement			
Resolution (Å)	135.34-3.32	235.61-3.63	234.98-3.34
No. reflections	123,065	81,274	89,539
<i>R</i> _{work} / <i>R</i> _{free} (%)	23.5/27.9	27.7/32.3	25.6/30.1
No. atoms			
Protein	67,232	67,760	70,549
Ligand/ion	0	0	0
Water	0	0	0
B-factors (Å ²)			
Protein	117.0	101.0	78.0
Ligand/ion	-	-	-
Water	-	-	-
R.m.s. deviations			
Bond lengths (Å)	0.002	0.003	0.002
Bond angles (°)	0.62	0.71	0.62

* Values in parentheses are for highest-resolution shell.
Number of crystals used for each dataset: 4 (6QNW), 1 (6QPF), and 2 (6QPG).

Extended Table 2
Cryo-EM data collection, refinement and validation
statistics

	FluPol _A -cRNA		FluPol _A -cRNA-Nb8205		FluPol _B -cRNA	Flu Pol _A -vRNA
	Dimer		Monomer	Dimer	Monomer	Monomer
	EMD-4664	EMD-4663	EMD-4661	EMD-4666	EMD-4660	EMD-4986
	PDB 6QX8	PDB 6QX3	PDB 6QXE	PDB 6QWL	PDB 6RR7	
Data collection and processing						
Magnification	130,000		130,000		130,000	130,000
Voltage (kV)	300		300		300	300
Electron exposure (e ⁻ /Å ²)	32.92		30.00		31.10	36.60
Defocus range (μm)	-0.5 to -0.7		-0.5 to -0.7		-1.3 to -2.5	-0.5
Pixel size (Å)	1.043		1.080		1.080	1.085
Symmetry imposed	C1	C2	C1	C1	C1	C1
Initial particle images (no.)	56,070		505,860	406,945	1,012,085	2,210,168
Final particle images (no.)	36,913		52,932	27,861	41,549	170,144
Map resolution (Å)	4.34	4.07	3.79	4.15	4.18	3.01
(FSC threshold 0.143)						
Map resolution range (Å)	3.97-7.82	3.84-6.35	3.70-5.41	3.85-7.43	3.90-6.30	2.82-5.03
3DFSC sphericity*	0.758	0.787	0.851	0.772	0.781	0.909
CryoEF score**	0.41	0.53	0.72	0.50	0.68	0.50
Refinement						
Initial model used (PDB code)	-	6QNW	6QPG	6QX8/6QPG	5EPI	6QNW
Model resolution (Å)	4.34	4.07	3.79	4.15	4.18	3.01
(FSC threshold 0.143)						
Model resolution range (Å)	3.97-7.82	3.84-6.35	3.70-5.41	3.85-7.43	3.90-6.30	2.82-5.03
Map sharpening <i>B</i> factor (Å ²)	-80	-100	-110	-95	-57	-65
Model composition						
Non-hydrogen atoms	-	38,596	21,589	-	10,409	36,306
Protein residues	-	2,384	1,337	-	1,244	2,228
Nucleotide (RNA)	-	24	14	-	26	30
<i>B</i> factors (Å²)						
Protein	-	68.60	71.24	-	151.24	22.39
Nucleotide (RNA)	-	64.94	86.46	-	207.12	24.68
R.m.s. deviations						
Bond lengths (Å)	-	0.007	0.004	-	0.008	0.007

	FluPol _A -cRNA		FluPol _A -cRNA-Nb8205		FluPol _B -cRNA	Flu Pol _A -vRNA
	Dimer		Monomer	Dimer	Monomer	Monomer
	EMD-4664	EMD-4663	EMD-4661	EMD-4666	EMD-4660	EMD-4986
	PDB 6QX8	PDB 6QX3	PDB 6QXE	PDB 6QWL	PDB 6RR7	
Bond angles (°)	-	1.158	0.750	-	1.006	0.820
Validation						
MolProbity score	-	1.85	1.66	-	2.10	1.31
Clashscore	-	6.48	3.24	-	10.07	1.90
Poor rotamers (%)	-	0.14	0	-	0.93	0
Ramachandran plot						
Favored (%)	-	91.86	90.34	-	89.07	94.88
Allowed (%)	-	7.97	9.66	-	10.85	5.12
Disallowed (%)	-	0.17	0	-	0.08	0

* Sphericity score calculated from 3D FSC curves⁶⁷.

** Efficiency score calculated from cryoEF⁶⁸.

Supplementary Material

Refer to Web version on PubMed Central for supplementary material.

Acknowledgements

We thank G.G. Brownlee and F. Vreede for plasmids, I. Berger for the MultiBac system and S. Cusack for sharing and discussing unpublished data on the 3' promoter binding site. We thank K. Harlos and T. Walter for assistance with crystallisation and K. Dent and D. Clare for cryo-EM assistance. We thank G.G. Brownlee, D. Stuart, and A. te Velthuis, as well as members of the Fodor and Grimes laboratories, for helpful comments and discussions. We thank Instruct-ERIC, part of the European Strategy Forum on Research Infrastructures (ESFRI), Instruct-ULTRA (EU H2020 Grant 731005), and the Research Foundation - Flanders (FWO) for support with nanobody discovery. This work was supported by Medical Research Council (MRC) programme grants MR/K000241/1 and MR/R009945/1 (to E.F.), Wellcome Investigator Award 200835/Z/16/Z (to J.M.G.), MRC Studentships (to A.P.W. and I.S.M.), Wellcome Studentship 092931/Z/10/Z (to N.H.). The authors would like to thank Diamond Light source for beamtime (proposals MX10627, MX14744, and MX19946), and for access and support of the cryo-EM facilities at the UK national Electron Bio-Imaging Centre (eBIC) (proposal EM14856), funded by the Wellcome, MRC and BBSRC. Further EM provision was provided through the OPIC electron microscopy facility which was founded by a Wellcome JIF award (060208/Z/00/Z) and is supported by a Wellcome equipment grant (093305/Z/10/Z). Computation used the Oxford Biomedical Research Computing (BMRC) facility, a joint development between the Wellcome Centre for Human Genetics and the Big Data Institute supported by Health Data Research UK and the NIHR Oxford Biomedical Research Centre. Financial support was provided by a Wellcome Trust Core Award (203141/Z/16/Z). The views expressed are those of the author(s) and not necessarily those of the NHS, the NIHR or the Department of Health. Part of this work was supported by Wellcome administrative support grant 203141/Z/16/Z.

Data availability

All data are available from the corresponding authors and/or included in the manuscript or Supplementary Information. Atomic coordinates have been deposited in the Protein Data Bank with accession codes 6QNW (H3N2 FluPol_A), 6QPF (H5N1 FluPol_A) and 6QPG (H3N2 FluPol_A+Nb8205). Cryo-EM density maps have been deposited in the Electron Microscopy Data Bank with accession codes EMD-4661 (monomeric H3N2 FluPol_A+cRNA +Nb8205), EMD-4663 and 4664 (dimeric H3N2 FluPol_A+cRNA), EMD-4666 (dimeric

H3N2 FluPol_A+cRNA+Nb8205), EMD-4660 (monomeric FluPol_B+cRNA), and EMD-4986 (monomeric H3N2 FluPol_A+vRNA+capped RNA) with the corresponding atomic coordinates deposited in the Protein Data Bank with accession numbers 6QX3, 6QX8, 6QXE, 6QWL, 6RR7, respectively.

References

1. Taubenberger JK, Kash JC. Influenza virus evolution, host adaptation, and pandemic formation. *Cell Host Microbe*. 2010; 7:440–51. [PubMed: 20542248]
2. Mostafa A, Abdelwhab EM, Mettenleiter TC, Pleschka S. Zoonotic Potential of Influenza A Viruses: A Comprehensive Overview. *Viruses*. 2018; 10
3. Pflug A, Lukarska M, Resa-Infante P, Reich S, Cusack S. Structural insights into RNA synthesis by the influenza virus transcription-replication machine. *Virus Res*. 2017; 234:103–117. [PubMed: 28115197]
4. Te Velthuis AJ, Fodor E. Influenza virus RNA polymerase: insights into the mechanisms of viral RNA synthesis. *Nat Rev Microbiol*. 2016; 14:479–93. [PubMed: 27396566]
5. Walker AP, Fodor E. Interplay between Influenza Virus and the Host RNA Polymerase II Transcriptional Machinery. *Trends Microbiol*. 2019; 27:398–407. [PubMed: 30642766]
6. Pflug A, Guilligay D, Reich S, Cusack S. Structure of influenza A polymerase bound to the viral RNA promoter. *Nature*. 2014; 516:355–60. [PubMed: 25409142]
7. Jorba N, Coloma R, Ortin J. Genetic trans-complementation establishes a new model for influenza virus RNA transcription and replication. *PLoS Pathog*. 2009; 5:e1000462. [PubMed: 19478885]
8. York A, Hengrung N, Vreede FT, Huiskonen JT, Fodor E. Isolation and characterization of the positive-sense replicative intermediate of a negative-strand RNA virus. *Proc Natl Acad Sci U S A*. 2013; 110:E4238–E4245. [PubMed: 24145413]
9. Jorba N, Area E, Ortin J. Oligomerization of the influenza virus polymerase complex in vivo. *J Gen Virol*. 2008; 89:520–4. [PubMed: 18198383]
10. Moeller A, Kirchdoerfer RN, Potter CS, Carragher B, Wilson IA. Organization of the influenza virus replication machinery. *Science*. 2012; 338:1631–4. [PubMed: 23180774]
11. Chang S, et al. Cryo-EM structure of influenza virus RNA polymerase complex at 4.3 Å resolution. *Mol Cell*. 2015; 57:925–935. [PubMed: 25620561]
12. Hara K, Schmidt FI, Crow M, Brownlee GG Amino acid residues in the N-terminal region of the PA subunit of influenza A virus RNA polymerase play a critical role in protein stability, endonuclease activity, cap binding, and virion RNA promoter binding. *J Virol*. 2006; 80:7789–98. [PubMed: 16873236]
13. Manz B, Brunotte L, Reuther P, Schwemmle M. Adaptive mutations in NEP compensate for defective H5N1 RNA replication in cultured human cells. *Nat Commun*. 2012; 3:802. [PubMed: 22549831]
14. Deng T, Vreede FT, Brownlee GG Different de novo initiation strategies are used by influenza virus RNA polymerase on its cRNA and viral RNA promoters during viral RNA replication. *J Virol*. 2006; 80:2337–48. [PubMed: 16474140]
15. Hengrung N, et al. Crystal structure of the RNA-dependent RNA polymerase from influenza C virus. *Nature*. 2015; 527:114–7. [PubMed: 26503046]
16. Thierry E, et al. Influenza Polymerase Can Adopt an Alternative Configuration Involving a Radical Repacking of PB2 Domains. *Mol Cell*. 2016; 61:125–37. [PubMed: 26711008]
17. Serna Martin I, et al. A Mechanism for the Activation of the Influenza Virus Transcriptase. *Mol Cell*. 2018; 70:1101–1110 e4. [PubMed: 29910112]
18. Reich S, et al. Structural insight into cap-snatching and RNA synthesis by influenza polymerase. *Nature*. 2014; 516:3616.
19. Gerlach P, Malet H, Cusack S, Reguera J. Structural Insights into Bunyavirus Replication and Its Regulation by the vRNA Promoter. *Cell*. 2015; 161:1267–79. [PubMed: 26004069]

20. Oymans J, Te Velthuis AJW. A Mechanism for Priming and Realignment during Influenza A Virus Replication. *J Virol*. 2018; 92
21. Te Velthuis AJ, Robb NC, Kapanidis AN, Fodor E. The role of the priming loop in influenza A virus RNA synthesis. *Nat Microbiol*. 2016; 1
22. Killip MJ, Fodor E, Randall RE. Influenza virus activation of the interferon system. *Virus Res*. 2015; 209:11–22. [PubMed: 25678267]
23. Te Velthuis AJW, et al. Mini viral RNAs act as innate immune agonists during influenza virus infection. *Nat Microbiol*. 2018; 3:1234–1242. [PubMed: 30224800]
24. Bieniossek C, Imasaki T, Takagi Y, Berger I. MultiBac: expanding the research toolbox for multiprotein complexes. *Trends in Biochemical Sciences*. 2012; 37:4957.
25. Weissmann F, et al. biGBac enables rapid gene assembly for the expression of large multisubunit protein complexes. *Proc Natl Acad Sci U S A*. 2016; 113:E2564–9. [PubMed: 27114506]
26. Pardon E, et al. A general protocol for the generation of Nanobodies for structural biology. *Nat Protoc*. 2014; 9
27. Walter TS, et al. A procedure for setting up high-throughput nanolitre crystallization experiments. Crystallization workflow for initial screening, automated storage, imaging and optimization. *Acta Crystallographica Section D-Biological Crystallography*. 2005; 61
28. Kabsch W. Xds. *Acta Crystallogr D Biol Crystallogr*. 2010; 66
29. Tickle, IJ, , et al. STARANISO. Cambridge, United Kingdom: Global Phasing Ltd; 2018. (<http://staraniso.globalphasing.org/cgi-bin/staraniso.cgi>)
30. McCoy AJ, et al. Phaser crystallographic software. *Journal of Applied Crystallography*. 2007; 40
31. Adams PD, et al. PHENIX: a comprehensive Python-based system for macromolecular structure solution. *Acta Crystallographica Section D-Biological Crystallography*. 2010; 66:213–221.
32. Emsley P, Cowtan K. Coot: model-building tools for molecular graphics. *Acta Crystallographica Section D-Biological Crystallography*. 2004; 60:2126–2132.
33. Smart OS, et al. Exploiting structure similarity in refinement: automated NCS and target-structure restraints in BUSTER. *Acta Crystallogr D Biol Crystallogr*. 2012; 68:368–80. [PubMed: 22505257]
34. Rasmussen SG, et al. Crystal structure of the beta2 adrenergic receptor-Gs protein complex. *Nature*. 2011; 477:549–55. [PubMed: 21772288]
35. Zheng SQ, et al. MotionCor2: anisotropic correction of beam-induced motion for improved cryo-electron microscopy. *Nat Methods*. 2017; 14:331–332. [PubMed: 28250466]
36. Zhang K. Gctf: Real-time CTF determination and correction. *J Struct Biol*. 2016; 193:1–12. [PubMed: 26592709]
37. Scheres SH. RELION: implementation of a Bayesian approach to cryo-EM structure determination. *J Struct Biol*. 2012; 180:519–30. [PubMed: 23000701]
38. Punjani A, Rubinstein JL, Fleet DJ, Brubaker MA. cryoSPARC: algorithms for rapid unsupervised cryo-EM structure determination. *Nat Methods*. 2017; 14:290–296. [PubMed: 28165473]
39. Pettersen EF, et al. UCSF Chimera--a visualization system for exploratory research and analysis. *J Comput Chem*. 2004; 25:1605–12. [PubMed: 15264254]
40. Emsley P, Lohkamp B, Scott WG, Cowtan K. Features and development of Coot. *Acta Crystallogr D Biol Crystallogr*. 2010; 66:486–501. [PubMed: 20383002]
41. Davis IW, et al. MolProbity: all-atom contacts and structure validation for proteins and nucleic acids. *Nucleic Acids Res*. 2007; 35:W375–83. [PubMed: 17452350]
42. Shkumatov AV, Strelkov SV. DATASW, a tool for HPLC-SAXS data analysis. *Acta Crystallogr D Biol Crystallogr*. 2015; 71:1347–50. [PubMed: 26057674]
43. Deng T, Sharps J, Fodor E, Brownlee GG. In vitro assembly of PB2 with a PB1-PA dimer supports a new model of assembly of influenza A virus polymerase subunits into a functional trimeric complex. *J Virol*. 2005; 79:8669–74. [PubMed: 15956611]
44. Fodor E, et al. A single amino acid mutation in the PA subunit of the influenza virus RNA polymerase inhibits endonucleolytic cleavage of capped RNAs. *J Virol*. 2002; 76:8989–9001. [PubMed: 12186883]

45. Fodor E, et al. Rescue of influenza A virus from recombinant DNA. *J Virol.* 1999; 73:9679–82. [PubMed: 10516084]
46. Fodor E, Smith M. The PA subunit is required for efficient nuclear accumulation of the PB1 subunit of the influenza A virus RNA polymerase complex. *J Virol.* 2004; 78:9144–53. [PubMed: 15308710]
47. Vreede FT, Jung TE, Brownlee GG. Brownlee GG Model suggesting that replication of influenza virus is regulated by stabilization of replicative intermediates. *J Virol.* 2004; 78:9568–72. [PubMed: 15308750]
48. Nilsson-Payant BE, Sharps J, Hengrung N, Fodor E. The Surface-Exposed PA(51-72)-Loop of the Influenza A Virus Polymerase Is Required for Viral Genome Replication. *J Virol.* 2018; 92
49. Schneider CA, Rasband WS, Eliceiri KW. NIH Image to ImageJ: 25 years of image analysis. *Nat Methods.* 2012; 9:671–5. [PubMed: 22930834]
50. Robb NC, Smith M, Vreede FT, Fodor E. NS2/NEP protein regulates transcription and replication of the influenza virus RNA genome. *J Gen Virol.* 2009; 90:1398–407. [PubMed: 19264657]
51. Reich S, Guilligay D, Cusack S. An in vitro fluorescence based study of initiation of RNA synthesis by influenza B polymerase. *Nucleic Acids Res.* 2017; 45:3353–3368. [PubMed: 28126917]
52. Bussey KA, et al. PA residues in the 2009 H1N1 pandemic influenza virus enhance avian influenza virus polymerase activity in mammalian cells. *J Virol.* 2011; 85:7020–8. [PubMed: 21561908]
53. Hu J, et al. The PA-gene-mediated lethal dissemination and excessive innate immune response contribute to the high virulence of H5N1 avian influenza virus in mice. *J Virol.* 2013; 87:2660–72. [PubMed: 23255810]
54. Ilyushina NA, et al. Adaptation of pandemic H1N1 influenza viruses in mice. *J Virol.* 2010; 84:8607–16. [PubMed: 20592084]
55. Kamiki H, et al. A PB1-K577E Mutation in H9N2 Influenza Virus Increases Polymerase Activity and Pathogenicity in Mice. *Viruses.* 2018; 10
56. Lee CY, et al. Novel mutations in avian PA in combination with an adaptive mutation in PR8 NP exacerbate the virulence of PR8-derived recombinant influenza A viruses in mice. *Vet Microbiol.* 2018; 221:114–121. [PubMed: 29981696]
57. Liedmann S, et al. New virulence determinants contribute to the enhanced immune response and reduced virulence of an influenza A virus A/PR8/34 variant. *J Infect Dis.* 2014; 209:532–41. [PubMed: 23983213]
58. Mehle A, Dugan VG, Taubenberger JK, Doudna JA. Reassortment and mutation of the avian influenza virus polymerase PA subunit overcome species barriers. *J Virol.* 2012; 86:1750–7. [PubMed: 22090127]
59. Neumann G, Macken CA, Kawaoka Y. Identification of amino acid changes that may have been critical for the genesis of A(H7N9) influenza viruses. *J Virol.* 2014; 88:4877–96. [PubMed: 24522919]
60. Peng X, et al. Amino Acid Substitutions HA A150V, PA A343T, and PB2 E627K Increase the Virulence of H5N6 Influenza Virus in Mice. *Front Microbiol.* 2018; 9:453. [PubMed: 29593694]
61. Slaine PD, et al. Adaptive Mutations in Influenza A/California/07/2009 Enhance Polymerase Activity and Infectious Virion Production. *Viruses.* 2018; 10
62. Wu R, et al. Multiple amino acid substitutions are involved in the adaptation of H9N2 avian influenza virus to mice. *Vet Microbiol.* 2009; 138:85–91. [PubMed: 19342184]
63. Xu G, et al. Prevailing PA Mutation K356R in Avian Influenza H9N2 Virus Increases Mammalian Replication and Pathogenicity. *J Virol.* 2016; 90:8105–14. [PubMed: 27384648]
64. Yamaji R, et al. Mammalian adaptive mutations of the PA protein of highly pathogenic avian H5N1 influenza virus. *J Virol.* 2015; 89:4117–25. [PubMed: 25631084]
65. Zhang Z, et al. Multiple amino acid substitutions involved in enhanced pathogenicity of LPAI H9N2 in mice. *Infect Genet Evol.* 2011; 11:1790–7. [PubMed: 21896338]
66. Zhong G, et al. Mutations in the PA Protein of Avian H5N1 Influenza Viruses Affect Polymerase Activity and Mouse Virulence. *J Virol.* 2018; 92

67. Tan YZ, et al. Addressing preferred specimen orientation in single-particle cryo-EM through tilting. *Nat Methods*. 2017; 14:793–796. [PubMed: 28671674]
68. Naydenova K, Russo CJ. Measuring the effects of particle orientation to improve the efficiency of electron cryomicroscopy. *Nat Commun*. 2017; 8:629. [PubMed: 28931821]

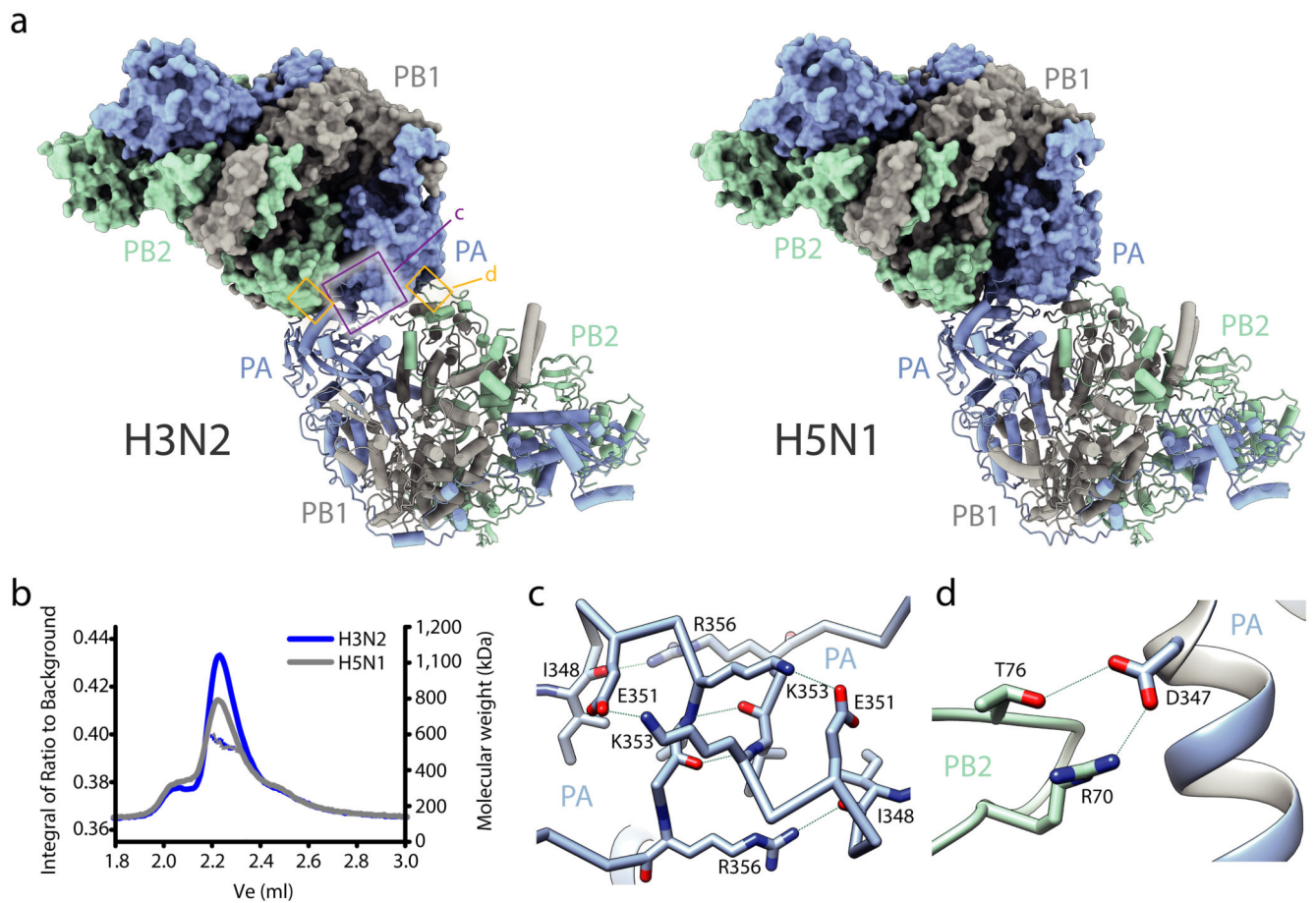


Fig. 1. Structures of human H3N2 and avian H5N1 FluPol_A.

a, Crystal structures of dimers of FluPol_A heterotrimers from human H3N2 (left) and avian H5N1 (right) influenza A viruses. Regions at the dimer interface (shown in close-up in panels **c** and **d**) are boxed. **b**, SEC-SAXS analysis of human H3N2 and avian H5N1 FluPol_A (n=3 independent experiments for H3N2 with similar results and n=1 for H5N1). Smooth lines reflect the relative UV signal of SEC and dotted lines indicate estimated molecular weight for each frame. Note that monomeric FluPol_A heterotrimer has an approximate molecular weight of 255 kDa. **c**, **d**, Interactions between loops 352-356 of the PA C-terminal domains (**c**) and the PA C-terminal domain and PB2 N1 subdomain (**d**) at the FluPol_A dimer interface. Dashed lines indicate hydrogen bonds.

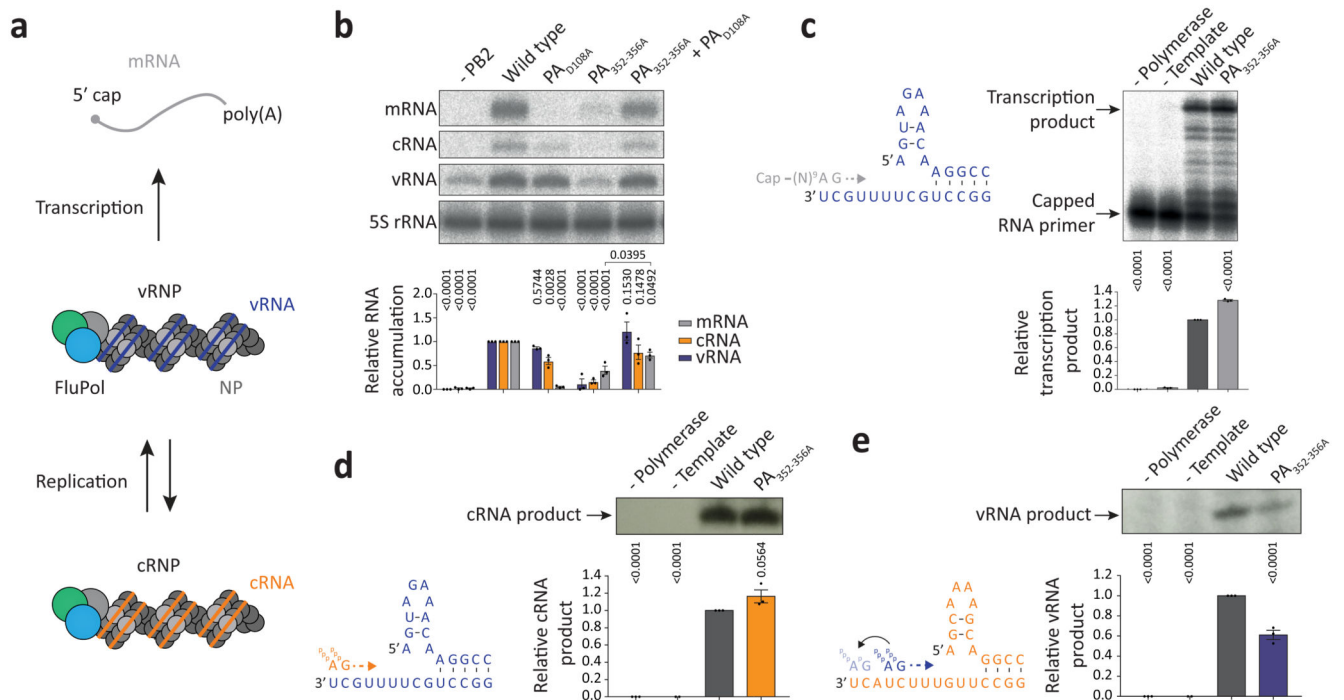


Fig. 2. Mutations at the FluPol_A dimer interface inhibit cRNA to vRNA replication.

a, Scheme of transcription and replication by FluPol_A in the context of viral ribonucleoproteins (vRNPs). **b**, vRNP reconstitution assay with the PA_{352-356A} dimer mutant and complementation with the transcription-deficient PA_{D108A} mutant. Data are mean ± s.e.m., n=3 independent transfections. Two-way ANOVA. $P < 0.05$ is considered significant. mRNA signals for PA_{352-356A} with and without PA_{D108A} were compared by two-tailed unpaired *t*-test. $P < 0.05$ is considered significant. **c**, Effect of the PA_{352-356A} mutation on *in vitro* transcription by FluPol_A primed with a capped RNA primer. Data are mean ± s.e.m., n=3 independent reactions. One-way ANOVA. $P < 0.05$ is considered significant. **d**, **e**, Effect of the PA_{352-356A} mutation on *in vitro* primer-independent replication by FluPol_A on a vRNA (**d**) and cRNA (**e**) template. Data are mean ± s.e.m., n=3 independent reactions. One-way ANOVA. $P < 0.05$ is considered significant. For gel source data, see Supplementary Fig. 2.

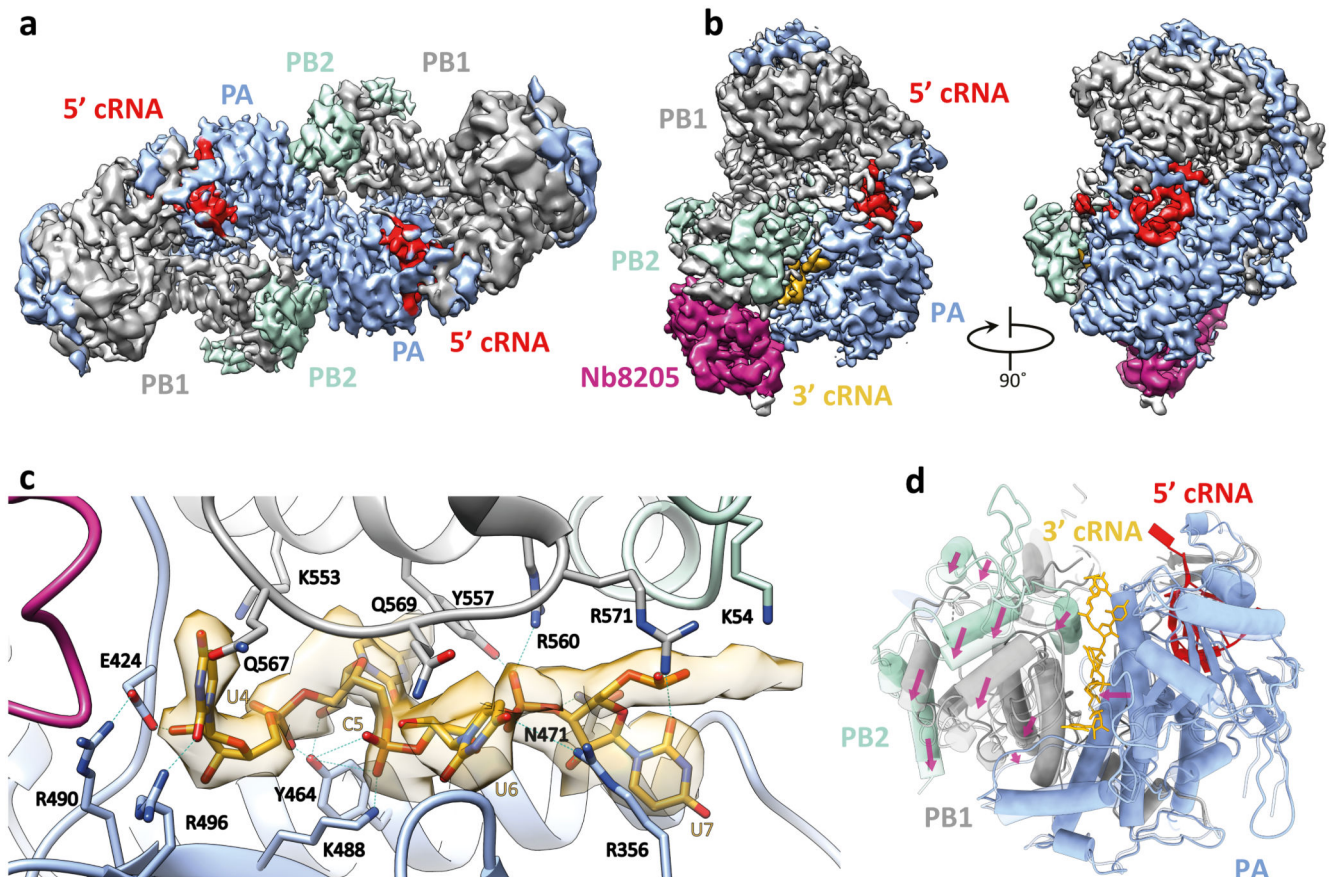


Fig. 3. Structures of H3N2 FluPol_A bound to cRNA promoter.

a, Cryo-EM map of dimer of FluPol_A heterotrimers bound to cRNA promoter. **b**, Cryo-EM map of cRNA-bound FluPol_A heterotrimer in complex with Nb8205. **c**, Close-up view of 3' cRNA binding site. **d**, Comparison between monomeric (full colour) and dimeric (transparency) FluPol_A polymerase reveals movement of the PB1 thumb/PB2 N1 subdomains (indicated by purple arrows) triggered by FluPol_A dimerisation, resulting in the opening of the 3' cRNA binding site.

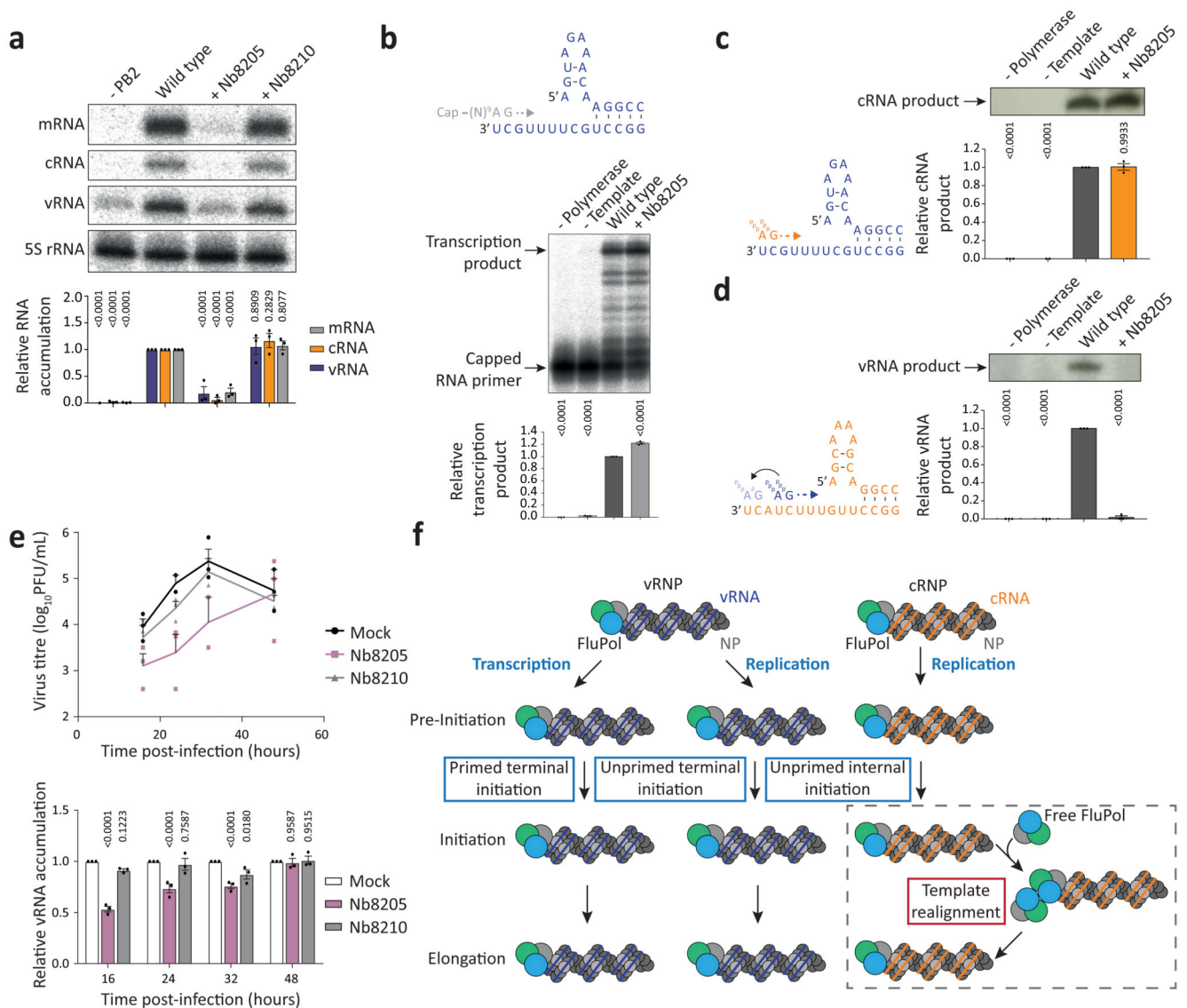


Fig. 4. Nanobody Nb8205 that binds FluPol_A at the dimer interface inhibits cRNA to vRNA replication and virus growth.

a, Effect of nanobodies on FluPol_A activity in a vRNP reconstitution assay. Data are mean \pm s.e.m., $n=3$ independent transfections. Two-way ANOVA. $P < 0.05$ is considered significant.

b, Effect of nanobody on *in vitro* transcription by FluPol_A primed with a capped RNA primer. Data are mean \pm s.e.m., $n=3$ independent reactions. One-way ANOVA. $P < 0.05$ is considered significant.

c, d, Effect of nanobody on *in vitro* primer-independent replication by FluPol_A on a vRNA (**c**) and cRNA (**d**) template. Data are mean \pm s.e.m., $n=3$ independent reactions. One-way ANOVA. $P < 0.05$ is considered significant.

e, Effect of nanobodies on the growth of influenza A/WSN/33 virus and vRNA levels in infected HEK-293T cells. Data are mean \pm s.e.m., $n=3$ independent transfections and infections. Two-way ANOVA (Nb8210: $P = 0.8126$; 0.4390 ; 0.8496 ; 0.8489 , Nb8205: $P = 0.1075$; 0.0096 ; 0.0217 ; 0.9828 , for 16, 24, 32, 48 hours post-infection). $P < 0.05$ is considered significant. For gel source

data, see Supplementary Fig. 2. **f**, Model for the role of polymerase dimerisation in influenza virus genome replication.